

27 Al(d,alpha) and 27 Al(d,p) Nuclear Reaction Cross Sections at $E_d < 2\text{MeV}$ Measured at Three Backward Scattering Angles Related to NRA

M. Salimi

K.N. Toosi University of Technology

O. Kakuee

NSTRI

S. F. Masoudi (✉ masoudi@kntu.ac.ir)

K.N. Toosi University of Technology

H. R. kheiri

NSTRI

E. Briand

Sorbonne Université, CNRS, Institut des NanoSciences de Paris, INSP, SAFIR

J-J. Ganem

Sorbonne Université, CNRS, Institut des NanoSciences de Paris, INSP, SAFIR

I. Vickridge

Sorbonne Université, CNRS, Institut des NanoSciences de Paris, INSP, SAFIR

Research Article

Keywords: nuclear reactions, ion beam analysis, spectra , SIMNRA

Posted Date: June 3rd, 2021

DOI: <https://doi.org/10.21203/rs.3.rs-574105/v1>

License: © ⓘ This work is licensed under a Creative Commons Attribution 4.0 International License.

[Read Full License](#)

$^{27}\text{Al}(\text{d},\alpha)$ and $^{27}\text{Al}(\text{d},\text{p})$ nuclear reaction cross sections at $E_{\text{d}} < 2\text{MeV}$ measured at three backward scattering angles related to NRA

M. Salimi^{1,2}, O. Kakuee³, S.F. Masoudi^{1,*}, H. Rafi kheiri³, E. Briand², J-J. Ganem², I. Vickridge²

¹ Department of Physics, K.N. Toosi University of Technology, P.O. Box 15875-4416, Tehran, Iran

² Sorbonne Université, CNRS, Institut des NanoSciences de Paris, INSP, SAFIR, F-75005 Paris, France

³ Physics and Accelerators Research School, NSTRI, PO Box 14395-836, Tehran, Iran

Abstract:

The cross-sections of deuteron-induced nuclear reactions suitable for ion beam analysis, measured in different laboratories, are often significantly different. In the present work, differential cross-sections of $^{27}\text{Al}(\text{d},\text{p})$ and $^{27}\text{Al}(\text{d},\alpha)$ reactions were measured, and the cross sections benchmarked with thick target spectra obtained from pure aluminium for the first time in two independent laboratories. The $^{27}\text{Al}(\text{d},\text{p})$ and (d,α) differential cross-sections were measured between 1.4 and 2 MeV at scattering angles of 165° , 150° , and 135° in the VDGT laboratory in Tehran (Iran), and the same measurements for detector angle of 150° were repeated from scratch, including target making, with independent equipment on the SAFIR platform at INSP in Paris (France). The results of these two measurements at 150° are in good agreement, and for the first time a fitted function is proposed to describe the Al-cross sections for which no suitable theoretical expression exists. The obtained differential cross-sections were validated through benchmarking, by fitting with SIMNRA deuteron-induced particle spectra obtained from a high purity bulk Al target at both labs for deuteron incident energies between 1.6 and 2 MeV. The thick target spectra are well-reproduced. The evaluated and benchmarked cross sections have been uploaded to the ion beam analysis nuclear data library database (www-nds.iaea.org/ibandl/).

* Corresponding author: masoudi@kntu.ac.ir

1- Introduction:

Ion beam analysis (IBA) has been widely used to analyze quantitatively and with high sensitivity the composition and elemental depth profiles in the surface regions of solids. For light element analysis, suitable nuclear reactions can be found and in particular, deuteron-induced reactions, (d,p) or (d, α), often have high Q-values and appreciable cross-sections. In many cases of Nuclear Reaction Analysis (NRA) of thin films, isolated reaction particle peaks may be obtained with judicious choice of scattering angle, incident beam energy, and filtering foils in front of the charged particle detector. However, in general, NRA generates complex spectra with overlapping peaks, especially from thick samples. Knowledge of the cross-sections for the cases of isolated peaks is already useful for designing experiments to determine elemental contents of thin films. Many such cross-sections, for example $^{16}\text{O}(d,p_0)^{17}\text{O}$, $^{16}\text{O}(d,p_1)^{17}\text{O}$, $^{12}\text{C}(d,p_0)$, $^{14}\text{N}(d,\alpha_0)$, have been carefully measured at energy and angular ranges of analytical interest [1-4]. It is sometimes possible to analyse several light elements simultaneously by NRA. Knowledge of the cross-sections of reactions that are not necessarily of primary interest for thin film analysis, is then often needed for cases in which targets contain elements giving rise to reactions that produce particle groups that interfere with the primary analytical peak, and even more so in thick target NRA where the broadening of the particle spectra from the non-zero target thickness leads to a much greater probability of elemental interferences. Furthermore, accurate experimental nuclear reaction cross-sections are required to provide proper parameters for appropriate approximations and expressions of theoretical nuclear reaction mechanism models [5-7].

Because oxygen is the most abundant element in the earth's crust and because of the universal importance of oxides in earth sciences and materials science, accurate cross-sections for ^{16}O and ^{18}O nuclear reactions have been determined [1, 8]. The second most abundant element is silicon, and although it is an intermediate-mass element from the point of view of IBA, it also has nuclear reactions of analytical interest that have been determined [2, 9].

Aluminium is the third most abundant element that is widely used in industry for its mechanical and electrical properties, decorative applications, and its resistance to environmental aggression especially after suitable electrochemical passivation. Aluminium is also widely present in the alumina-silicate rocks that constitute so much of the earth's upper crust. In many thin film systems, such as III-Nitrogen semiconductors developed amongst other things for UV-C light emitting diodes destined to replace UV mercury lamps in mass sterilisation applications for COVID mitigation, and thin conformal alumina films or nanolaminates grown by Atomic Layer Deposition where aluminium is an essential component, absolute determination of the Al content is paramount for developing improved materials. There is a wealth of deuteron-induced

charged particle reactions on ^{27}Al with high Q-values that may be exploited in NRA for analysis of aluminum or encountered as interferences in NRA of aluminium-containing materials.[10-20]

There is a further motivation for good knowledge of Al cross sections: even if analysis of Al is not the main objective of a measurement, reaction products from Al may interfere with the signals from other reactions of interest and to be able to fully fit a complex NRA spectrum, all of the cross sections involved need to be known. Detailed knowledge of the cross-sections of these reactions is thus a significant interest in the field of NRA. The compound nucleus ^{29}Si contains too many close levels to be able to be treated satisfactorily within R-Matrix theory, and too few to be able to be handled satisfactorily with a statistical approach. At present, the best we can obtain is well measured experimental cross-sections[10-16].

The first measurements of $^{27}\text{Al}(d,\alpha)$ and $^{27}\text{Al}(d,p)$ cross-sections were made by Gadioli [21] at 150° as part of a study of the fluctuation mechanism occurring in the differential excitation functions. These cross-section curves have since been measured for deuteron energies less than 3 MeV at 90° , 135° , 150° , 165° , and 173° [10, 13-16, 21-23], however significant gaps and discrepancies remain.

In this work, we have determined the cross-sections for the $^{27}\text{Al}(d,p_{0+1,2+3,4,5+6,9,10,11,12})$ and $^{27}\text{Al}(d,\alpha_{0,1,2,3,4})$ reactions at an energy below 2 MeV and at 150° scattering angle in two completely independent measurements in two different laboratories: the Van De Graaff Lab in Tehran (VDGT) and the SAFIR platform of the Institut des NanoSciences de Paris (INSP). The $^{27}\text{Al}(d,p)$ and (d,α) cross-sections were also determined at 135° and 165° at VDG. From our measured data and a critical evaluation of previous measurements, we propose a set of recommended cross-sections for NRA and demonstrate their validity through benchmarking experiments in a thick pure aluminum target in both laboratories.

2- Experimental setup and procedure

The experimental setups at VDG and INSP are significantly different. We present here the main experimental features of each laboratory.

2-1- Experimental setup and procedure at VDG

2-1-1- Chamber and data acquisition

At VDG, cross sections and benchmarking spectra were measured in the 30° left beamline of the 3MV Van de Graaff electrostatic accelerator, equipped with a chamber developed for accurate and reliable RBS/NRA measurements[24]. A beam of 20-40nA was directed into a beam spot of $1.5 \times 1.5 \text{ mm}^2$. The

energy resolution is estimated to be about 1 keV. Under these conditions, deadtime was less than 10% and pileup was minimized.

The pressure of the chamber was about 2×10^{-6} mbar during the measurements. The detection system for all of the measurements consisted of three $25\text{mm}^2 \times 300 \mu\text{m}$ thick surface barrier detectors installed at 135° , 150° , and 165° degrees from the incident beam direction. The angular spread of each detector was less than 3° , with solid angles Ω of 1-2 msr. Integrated beam charge Q of $10 \mu\text{C}$ was usually sufficient to obtain adequate statistics.

2-1-2- Calibration energy of the accelerator:

We determined beam energy from the field strength of the analyzing magnet, measured with an NMR fluxmeter[25]. The energy calibration of the accelerator was determined from the reaction threshold energy at 1880.44 ± 0.02 keV in the ${}^7\text{Li}(p,n){}^7\text{Be}$ reaction. The target was a pressed LiF pellet with a $10 \mu\text{g}/\text{cm}^2$ silver coating for charge evacuation and neutrons were detected with a BF₃ detector.

2-1-3- Target preparation:

The thin Al target must be of appropriate thickness, stable both in atmosphere and under the beam in vacuum, and should also be amorphous to avoid unwanted channeling effects[26]. To achieve these requirements, physical vapor deposition (PVD) was chosen from amongst the different methods for thin Al target preparation[27]. Pure Al was evaporated onto a microscope slide which had been prepared by dipping into a mixture of water and detergent under ultrasonic agitation. The PVD system was a model VE-770 with a base pressure of about 10^{-6} mbar, equipped with a coiled tungsten filament. The obtained film was floated onto water and then fished over an 8mm diameter hole in a thin metal sheet. Finally, 10 ± 0.5 nm of Ag was deposited onto the thin self-supporting vacuum evaporated Al film as an internal reference[24, 28].

2-1-4- Characterization of the thin target

The thin target thickness is determined by RBS [29] with an uncertainty of less than 5%, due to uncertainties in $Q \times \Omega$, in possible deviations of the ${}^{27}\text{Al}(\alpha, \alpha){}^{27}\text{Al}$ cross section from the assumed Rutherford cross section and in fitting the simulated spectrum to the measured spectrum. The thickness of target was only used for determination of deuteron beam energy loss through the target. The thickness and stoichiometry of the Al/Au target were measured at the three detection angles of 135° , 150° , and 165° by alpha particle beams of 1.8 MeV. This measurement was simulated with SIMNRA 7.03 by using the Chu and Yang straggling model and Ziegler/Biersack stopping power [30]. Typical simulated and measured spectra are shown in Fig. 1.

Fig.1. Typical simulated and measured RBS spectra from a thin Al/Ag target obtained at scattering angle 150° and $E_\alpha = 1.8$ MeV.

In target characterization with the alpha beam, the areal density ratio $\frac{N_{Ag}}{N_{Al}}$ was calculated by equation [1]:

$$\frac{N_{Ag}}{N_{Al}} = \frac{Y_{Ag}}{Y_{Al}} \times \frac{\left(\frac{d\sigma}{d\Omega}\right)_{\theta, EBS, E=E_{Al}, \alpha}^{Al}}{\left(\frac{d\sigma}{d\Omega}\right)_{\theta, Ruth, E=E_{Ag}, \alpha}^{Ag}} \quad (1)$$

where N corresponds to the areal density of the target and Y to the experimental yield (net area under the peak). Here, N_A rather than $[A]$ is used to represent the areal density of species A, in order to simplify the expressions. The average of these ratios from different detection angles was estimated by assuming the Rutherford cross section for reaction of alpha particles with Ag and Al, and applying a correction for the

energy loss in the thin target. $\left(\frac{d\sigma}{d\Omega}\right)_{\theta, Ruth, E=E_{Ag}, \alpha}^{Ag}$ is defined as the Rutherford cross section at $E_{Ag, \alpha} = E_\alpha -$

$\frac{(\Delta E)_{\theta, E_\alpha}^{Ag}}{2}$ for $E_\alpha = 1.8$ MeV. The alpha particle elastic scattering cross section $\left(\frac{d\sigma}{d\Omega}\right)_{\theta, EBS, E=E_{Al}, \alpha}^{Al}$ can be

considered to be Rutherford for the energy $E_{Al, \alpha} = \overline{E_{Al}} - \frac{(\Delta E)_{\theta, E=\overline{E_{Al}}}^{Al}}{2}$; $\overline{E_{Al}} = E_\alpha - (\Delta E)_{\theta, E=E_\alpha}^{Ag}$, where E_α , $(\Delta E)_{\theta, E=\overline{E_{Al}}}^{Al}$ and $(\Delta E)_{\theta, E_\alpha}^{Ag}$ are the incident alpha energy, energy loss in the Al layer for $E = \overline{E_{Al}}$ and energy loss in Ag layer, respectively.

Using this ratio eliminates uncertainty due to solid angle, dead time, and charge measurement for the differential nuclear cross section measurements.

2-2- Experimental work in INSP Lab:

At INSP Lab in Paris, the 30° right beamline of the 2.5 MV Van de Graaff electrostatic accelerator of SAFIR (Système d'Analyse par Faisceaux d'Ions Rapides) platform was employed for our measurement.

The accelerator energy, read from the Generating Voltmeter signal, was calibrated by using the narrow nuclear resonances of the $^{27}\text{Al}(p, \gamma)^{28}\text{Si}$ reaction at 991.88 keV, the $^{13}\text{C}(p, \gamma)^{14}\text{N}$ reaction at 1747.6 keV and the $^{15}\text{N}(p, \alpha\gamma)^{12}\text{C}$ reaction at 426.1 keV. In each case, the gamma rays were detected with a BGO scintillation detector at 0° [31, 32]. Because of the very high energy resolution of the beam – less than 250eV full width half maximum energy spread over the range reported here, excitation curves were fitted with SPACES [33] so as to compensate for small distortions of the excitation curve due to surface contaminants and oxidation. The treatment of the GVM signal has been implemented into Labview rather than in analogue electronic circuits, giving an energy calibration that is highly linear and practically independent of temperature.

A similar method to that used at VDGT was employed at INSP for preparation of the thin self-supporting targets. An EDWARDS FL 400 and VINCI technologies PVD 4E were used for Al and Au evaporation respectively. The preparation – floating and fishing - and characterization of the target were the same as at VDGT Lab in Tehran, with the exception that here we have used Au rather than Ag as the internal standard for the INSP targets, and subsequently the areal density ratio was taken into account as $\frac{N_{Au}}{N_{Al}}$ in the differential cross section measurement. Also, absolute values of the areal densities N_{Al} and N_{Au} were determined by comparing with the standard Bi-implanted Si reference with an uncertainty of 2%–3% in the same RBS measurement. Scanning electron microscopy (SEM) images of the surface of from Au/Al target, shown in Fig. 2, confirmed the uniformity of the surface structure of samples at the nanoscale.

Fig. 2. SEM images of the surface of from Au/Al target

3- Data analysis and results:

3-1- The differential nuclear cross section measurement value at VDGT Lab in Tehran:

Among the nuclear reactions that can be used to characterize Al, $^{27}\text{Al}(d,p_{0+1,2+3,4,5+6,9,10,11,12})^{28}\text{Al}$ and $^{27}\text{Al}(d,\alpha_{0,1,2,3,4})^{25}\text{Mg}$ were selected for measurements of the deuteron induced reaction cross sections since these particle groups can be identified and their intensities estimated under reasonable experimental conditions. The cross sections were measured with 10 keV steps, for energies ranging from 1.3–2 MeV.

In order to discriminate between high Q-value (d,p) and (d, α) groups in a single measurement setup, we placed a 4 μm thick mylar filter in front of the detector. The judicious choice of mylar thickness, to minimize interferences in the thin target spectra, was found through SIMNRA simulations. The discrimination is illustrated in Fig. 3, comparing a real measured spectrum with 4 μm mylar, with a simulated spectrum without filter. Clearly, interference between the particles from $^{27}\text{Al}(d,p_{0+1})^{28}\text{Al}$ and $^{27}\text{Al}(d,\alpha_0)^{25}\text{Mg}$, and from $^{27}\text{Al}(d,p_4)^{28}\text{Al}$ and $^{27}\text{Al}(d,\alpha_3)^{25}\text{Mg}$ is eliminated.

Fig. 3. (a) The simulated spectrum without mylar and (b) the typical measured spectrum in experimental work with 4 μm mylar in front of the particle detector at the detection angle of 150° and for $E_{d,\text{lab}} = 1.8$ MeV at VDGT Lab in Tehran. The interferences between the high energy alpha and proton groups are clearly resolved.

The differential cross section values $\left(\frac{d\sigma}{d\Omega}\right)_{\theta,E(Al)}$ at the energy E_d and detection angle θ were obtained from

Eq. (2):

$$\left(\frac{d\sigma}{d\Omega}\right)_{\theta,E(Al)} = \left(\frac{d\sigma}{d\Omega}\right)_{\theta,EBS,E_d(Ag)}^{Ag} \times \frac{Y_{Al}}{Y_{Ag}} \times \frac{N_{Ag}}{N_{Al}} \times \frac{(Q \times \Omega)^{\theta,Ag}}{(Q \times \Omega)^{\theta,Al}} \quad (2)$$

where E_d , $Y_{Al\text{ or }Ag}$, θ and $(\Delta E)_{\theta,d}^{Ag}$ represent incident deuteron beam energy, the experimental yield of Al or Ag (net area under the peak), scattering angle and energy loss in Ag layer, respectively. $\left(\frac{d\sigma}{d\Omega}\right)_{\theta,EBS,E_d(Ag)}^{Ag}$ is the differential cross section of the $^{nat}Ag(d,d_0)$ reaction at $E_d(Ag) = E_{d,\theta} - \frac{(\Delta E)_{\theta,d}^{Ag}}{2}$, which is Rutherford below 2 MeV. $\frac{(Q \times \Omega)^{\theta,Ag}}{(Q \times \Omega)^{\theta,Al}}$ is equal to one since the charge (Q) and solid angle (Ω) for Al and Ag are identical at each scattering angle, eliminating the uncertainty due to Q and Ω measurement. Also, $\frac{N_{Ag}}{N_{Al}}$ was measured by RBS as explained above.

The measured excitation functions at VDGT Lab at scattering angle 150° for the $^{27}Al(d,\alpha_0-3)^{25}Mg$ and $^{27}Al(d,p_{0-12})^{28}Al$ reactions are displayed in Figs. 4 and 5 and the excitation functions for the $^{27}Al(d,\alpha)^{25}Mg$ and $^{27}Al(d,p)^{28}Al$ reactions at scattering angles 165° and 135° are shown in Figs. 6a, 6b, 7a and 7b. The only previous measurements of the $^{27}Al(d,\alpha)$ cross sections of which we are aware, apart from at 150° where there are several data sets that are discussed below, is that from [34] for 135° . This data is indicated on Fig. 7a, however the values are rather sparse and show significant fluctuations. They were not further used in the present work.

Fig. 4. The excitation functions at scattering angle 150° at VDGT Lab in Tehran for the $^{27}Al(d,\alpha)^{25}Mg$ reactions. The estimated uncertainties from counting statistics are smaller than the plotted symbols.

Fig. 5. Differential cross section values for the $^{27}Al(d,p_{0-12})^{28}Al$ reactions at scattering angle 150° at VDGT Lab in Tehran. The estimated uncertainties from counting statistics are smaller than the plotted symbols.

Fig. 6. The differential cross sections at 165° measured at VDGT Lab in Tehran for the (a) $^{27}Al(d,\alpha)^{25}Mg$ and (b) $^{27}Al(d,p)^{28}Al$ reactions. The estimated uncertainties from counting statistics are smaller than the plotted symbols.

Fig. 7. The differential cross sections measured at 135° at VDGT Lab in Tehran for the (a) $^{27}Al(d,\alpha)^{25}Mg$ reactions together with the data from [34], and (b) $^{27}Al(d,p)^{28}Al$ reactions. The estimated uncertainties from counting statistics are smaller than the plotted symbols.

3-2- The differential cross section measurement at INSP Lab in Paris:

The experiments were done with three different experimental setups, as follows: for (d,α) reaction measurements, we used the $4\mu\text{m}$ -thick mylar in front of the $300\mu\text{m}$ -thick surface barrier detector and

repeated these measurements without mylar in front of the detector. For (d,p) reaction measurements, in the third configuration, a 100µm-thick mylar was chosen in front of a 500 µm-thick pin diode detector at scattering angle of 150°. Typical experimental alpha particle and proton spectra from the $^{27}\text{Al}(d,\alpha)^{25}\text{Mg}$ and $^{27}\text{Al}(d,p)^{28}\text{Al}$ reactions are shown in Fig. 8-a and Fig. 9-a, respectively.

Fig. 8. (a) A typical spectrum of alpha-particles for the $^{27}\text{Al}(d,\alpha)^{25}\text{Mg}$ reaction, (b) The excitation functions for the $^{27}\text{Al}(d,\alpha)^{25}\text{Mg}$ reaction at scattering angle 150° at INSP Lab in Paris. The estimated uncertainties from counting statistics are smaller than the plotted symbols.

Fig. 9. (a) A typical spectrum of protons for the $^{27}\text{Al}(d,p)^{28}\text{Al}$ reaction. (b) The excitation functions for the $^{27}\text{Al}(d,p)^{28}\text{Al}$ reaction at scattering angle 150° at INSP Lab in Paris. Where not visible, the estimated uncertainties from counting statistics are smaller than the plotted symbols.

The differential cross-sections were determined by using equation [1], just replacing Ag by Au:

$$\left(\frac{d\sigma}{d\Omega}\right)_{\theta, E_d(Al)} = \left(\frac{d\sigma}{d\Omega}\right)_{\theta, EBS, E_d(Au)}^{Au} \times \frac{Y_{Al}}{Y_{Au}} \times \frac{N_{Au}}{N_{Al}} \quad (3)$$

where θ , Y_{Al} and Y_{Au} , $E_d(Au)$, $E_d(Al)$ correspond to the scattering angle, integrated yields (Au and Al) as obtained from the experimental spectra, the energy at the surface of the Au layer, and the energy at half of the Aluminium thickness (including energy loss in the Au film), respectively. $\frac{N_{Au}}{N_{Al}}$ represents the areal density of Au versus Al present in the target, measured by RBS.

3-3- Uncertainties

Using the measured $\frac{N_{Au}}{N_{Al}}$ ratio and normalizing the cross section measurement to the corresponding Rutherford cross-section, the uncertainties owing to solid angle, detector angular settings, dead time, and charge measurement were eliminated[35]. The uncertainty of the $\frac{N_{Au}}{N_{Al}}$ ratio was estimated to be about 3% according to the counting statistics. The corresponding statistical uncertainties of $\left(\frac{d\sigma}{d\Omega}\right)_{\theta, E_d(Al)}$ were estimated to be 4%-9% according to the error propagation formulas.

The measured differential cross section at INSP Lab with error bars at scattering angle 150° for the $^{27}\text{Al}(d,\alpha_0-3)^{25}\text{Mg}$ and $^{27}\text{Al}(d,p_{0-6})^{28}\text{Al}$ reactions are indicated in Fig. 8-b and Fig. 9-b.

4- Discussion

4-1- Correspondence between VDGT's data and INSP's data

Figure 10 shows the comparison between our data from VDGT and from INSP. The results show that the data acquired at INSP Lab in Paris for $^{27}\text{Al}(d,\alpha_{0,1,2,3,4})^{25}\text{Mg}$ and $^{27}\text{Al}(d,p_{0+1,2+3,4,5+6})^{28}\text{Al}$ are in acceptable agreement with data obtained at VDGT Lab at 150° scattering angle. Since these datasets were obtained under completely independent and somewhat different setups, this agreement is a strong indicator of the validity of the datasets.

Fig. 10. The comparison between our data from VDGT and from INSP at 150° for the (a) $^{27}\text{Al}(d,\alpha_{0,1,2,3,4})^{25}\text{Mg}$ and (b) $^{27}\text{Al}(d,p_{0+1,2+3,4,5+6})^{28}\text{Al}$ reactions.

4-2- Comparison with previous studies

Although we are not aware of previous measurements for 135° (other than [34], for (d,α) , discussed above) and 165° scattering angles, several data sets exist for 150° . Comparison of the cross sections measured here with available aluminum (d,p) and (d,α) cross-sections at 150° is presented in Fig. 11. As mentioned in [10], the measurements of Ref. [13] barely overlaps with previous studies, and the data from [16] are underestimated by a factor of about 2, so they are no longer considered here. The differential cross section values in Ref [21] show systematic differences from the other data, beyond the uncertainties given in the paper, both for $^{27}\text{Al}(d,p_{0+1,2+3,4,5+6})^{28}\text{Al}$ and $^{27}\text{Al}(d,\alpha_{0,1,2,3,4})^{25}\text{Mg}$. Data in Ref. [10] are in acceptable agreement with our data except for a small energy shift. We attribute this energy shift to the energy loss of the incident beam in the target, which was not taken into account in [10]. The four retained datasets have been plotted in Fig. 12 for the 150° scattering, with the data from Ref. [10] corrected for the energy loss in the target, using the target thickness supplied in that publication.

Fig. 11. The comparison of our work with other data at 150° for (a) $^{27}\text{Al}(d,\alpha_{0,1,2,3,4})^{25}\text{Mg}$ and (b) $^{27}\text{Al}(d,p_{0+1,2+3,4,5+6})^{28}\text{Al}$ reactions [10, 21].

4-3-Evaluation of 150° cross section measurements

Since there is no suitable nuclear reaction model for these reactions, the question arises as to how to represent the best averaged values of the data to propose a single recommended cross section at any energy within the measured range. We have taken the approach of fitting a freely chosen mathematical function to all of the data, weighted inversely according to their reported uncertainties.

The four retained datasets were therefore fitted with 8-term and 20-term Fourier series, and a spline interpolation algorithm, shown in Fig. 12.

The differences between the fitted functions are small but the 20-term Fourier series allows the data to be represented with good fidelity and not too many fitted parameters. This is shown in Fig. 13.

Fig. 12. The comparison of different fitting methods for cross sections at 150° for (a) $^{27}\text{Al}(d, \alpha_{0,1,2,3,4})^{25}\text{Mg}$ and (b) $^{27}\text{Al}(d, p_{0+1,2+3,4,5+6})^{28}\text{Al}$ reactions.

Fig. 13. The fitted data for 150° for (a) $^{27}\text{Al}(d, \alpha_{0,1,2,3,4})^{25}\text{Mg}$ and (b) $^{27}\text{Al}(d, p_{0+1,2+3,4,5+6})^{28}\text{Al}$ reactions.

4-3-1- Fourier series equations

One of the advantages of fitting the data with the Fourier series is that the theoretical function can be expressed easily and used as a reference model in future works. The actual Fourier series are written as follows[36]:

$$f(x) = a_0 + \sum_{\{n=1\}}^N a_n \cos(n\omega x) + b_n \sin(n\omega x) \quad (4)$$

Theoretically, the Fourier coefficients a_n and b_n can be evaluated as follows:

$$a_0 = \frac{1}{T} \int_T f(x) dx \quad (5)$$

$$a_n = \frac{2}{T} \int_T f(x) \cos(n\omega x) dx \quad (6)$$

$$b_n = \frac{2}{T} \int_T f(x) \sin(n\omega x) dx \quad (7)$$

Considering the N=20 Fourier series, the coefficients for all of the cross sections reported here (in addition to the 150° collection) were calculated and are presented in Table 1. The goodness of fit is given by the coefficient of correlation R which describes the proportion of the variation of the data described by the fitted function[37]. R^2 is above 0.96 for the highest cross sections, and above 0.9 even for the lower cross sections which are statistically noisier.

5- Benchmarking the Evaluated cross sections

The measured cross sections are validated by a benchmarking exercise[38, 39], in which the cross sections are used in an independent experiment. For NRA cross sections, this almost always consists in obtaining thick target NRA spectra from a well-defined (often mono-elemental) target and verifying the extent to which the measured cross sections reproduce the observed spectra when included in an established NRA

simulator such as SIMNRA. To our knowledge, only the $^{27}\text{Al}(d,p)^{28}\text{Al}$ cross-sections have been benchmarked, by obtaining and fitting thick target spectra, for just one incident energy and one scattering angle [10], whilst there have been no benchmarking experiments at all for $^{27}\text{Al}(d,\alpha)^{25}\text{Mg}$ cross sections.

The goal of the present work is to benchmark the $^{27}\text{Al}(d,p)^{28}\text{Al}$ and $^{27}\text{Al}(d,\alpha)^{25}\text{Mg}$ cross sections at three scattering angles, 135° , 150° , and 165° , and with various incident beam energies in two different laboratories.

For the experimental part of benchmarking, charged particle spectra were obtained from a thick pure aluminium target under deuteron irradiation. For the simulation part of benchmarking, the SIMNRA 7.03 code is applied with the Chu and Yang straggling model and Ziegler/Biersack stopping power.

5-1- Benchmarking of measured data for $^{27}\text{Al}(d,p)^{28}\text{Al}$ and $^{27}\text{Al}(d,\alpha)^{25}\text{Mg}$ reactions at VDGT Lab in Tehran

For benchmarking the $^{27}\text{Al}(d,p)^{28}\text{Al}$ and $^{27}\text{Al}(d,\alpha)^{25}\text{Mg}$ cross sections at VDGT Lab in Tehran, we used a thick pure Al target with a thin Ag layer deposited on it for the self-normalization process. No mylar was used in front of the detector. Other experimental parameters are as explained in section 2-1. The results of benchmarking for $E_d=1600-1900\text{keV}$ at the scattering angles of 135° , 150° and 165° , with an incident energy interval of 100keV , are shown in Fig. 14, Fig. 15, and Fig. 16, respectively. At 150° , the three cross section data sets (VDGT data, INSP data, and fitted data) have been incorporated into the SIMNRA library. Overall, the agreement between the simulated and measured spectra is satisfying.

Fig. 14. The benchmarking result at VDGT Lab in Tehran with different data sets and different incident deuteron energies at 150° .

Fig. 15. The benchmarking result at VDGT Lab in Tehran with measured VDGT data at different incident deuteron energies at 165° .

Fig. 16. The benchmarking result at VDGT Lab in Tehran with measured VDGT data with different incident deuteron energies at 135° .

5-2- Benchmarking of measured data for $^{27}\text{Al}(d,p)^{28}\text{Al}$ reactions at INSP Lab in Paris:

For benchmarking the $^{27}\text{Al}(d,p)^{28}\text{Al}$ cross sections at INSP Lab in Paris, Au rather than Ag deposited on the thick pure Aluminum target acted as the internal reference. Moreover, a new multi-holder detector at INSP lab was designed (Fig. 17), which included three 1cm^2 Hamamatsu S3590-09 PIN diodes, with

depletion depth of 300 μm , as detectors at 135°, 150° and 165°. A 100 μm mylar foil in front of each detector ensured the elimination of the alpha particles from the spectrum.

The benchmarking results are displayed in Fig. 18 for $E_d=1700\text{-}2000\text{keV}$ with an energy step of 100keV, at the scattering angle of 150° for VDGT data, INSP data, and fitted data sets. Figures 19 and 20 present the benchmarking results for $E_d=1500\text{-}1800\text{keV}$ with an energy step of 100keV at the scattering angles of 165° and 135°, respectively. The simulation at these angles employed the measured VDGT cross section data. In general, the correspondence between the simulations and the measured thick target spectra was very satisfying.

The range of measured cross-sections used for simulating the spectra was 1.4-2 MeV. After energy loss in the Al target, whenever $E_{d,\text{Lab}}$ falls below the minimum energy of the measured cross section (1.4 MeV), the corresponding simulation of measured cross-sections has no value and SIMNRA considers its value equal to zero. In this case, for the $^{27}\text{Al}(d,p_{0+1})$ reaction we manually inserted widely spaced cross section values for energies below 1.4 MeV so that the measured thick target spectra in the energy range from 4700-5000 keV were reproduced by the simulations. Similar inclusions were made for the $^{27}\text{Al}(d,p_{2+3}, p_4, p_{5+6})$ cross sections in the relevant energy ranges. These cross section values are certainly of the right amplitude, but because of the energy straggling of the incident beam at these depths in the target, in this energy range the proposed cross section would not faithfully represent any fine structure. In order to differentiate between the cross sections measured by the thin targets and incarnated by the N=20 Fourier series, from the values inferred from the benchmarking experiments, the two data sets are loaded separately into IBANDL.

6- Conclusions:

The $^{27}\text{Al}(d,p_{0+1,2+3,4,5+6})^{28}\text{Al}$ and $^{27}\text{Al}(d, \alpha_{0,1,2,3,4})^{25}\text{Mg}$ reaction cross sections were measured at VGDT (Tehran) on thin self-supporting aluminium targets for incident deuteron energies in the range 1.4 to 2 MeV at 135°, 150°, and 165° laboratory scattering angles. The measurements for 150° were independently repeated on the SAFIR platform at INSP and showed close agreement with the VDGT data. The cross sections at 150° were evaluated with existing data sets and an N=20 Fourier series fit is proposed to embody the evaluated cross section. The evaluated cross-sections have been benchmarked through a series of thick target spectra of charged particles induced by deuteron beams from a pure aluminium target, under various detection conditions at both VDGT and INSP. The overall agreement between the spectra simulated by SIMNRA and the measured benchmarking spectra is most satisfying and validates the evaluated cross sections presented here. We therefore recommend the use of these evaluated cross sections for use in NRA.

We note that the recommended cross sections for 135° and 165° are the first $^{27}\text{Al}(d,p)$ and $^{27}\text{Al}(d,\alpha)$ cross sections to be benchmarked at these angles for NRA.

7- Acknowledgements

We are particularly indebted to S. Steydli (INSP) for assistance in mechanical and vacuum aspects, and H. Tancrez (INSP) for electronic and command-control systems development. M. Salimi would also like to express her deep appreciation of the strong support of M. Marangolo (Director of INSP) and N. Witkowski (Directrice of the Doctoral School) for her co-tutelle doctoral contract. M. Salimi gratefully acknowledges the contribution from CAMPUS FRANCE in support of her co-tutelle doctoral contract.

8- References

1. Rafi-kheiri, H., Kakuee, O. & Lamehi-Rachti, M. Differential cross section measurement of $^{16}\text{O}(d, p0, 1)$ reactions at energies and angles relevant to nra. *Nucl. Instruments Methods Phys. Res. Sect. B: Beam Interactions with Mater. Atoms* **371**, 46–49 (2016).
2. Gurbich, A. & Molodtsov, S. Application of iba techniques to silicon profiling in protective oxide films on a steel surface. *Nucl. Instruments Methods Phys. Res. Sect. B: Beam Interactions with Mater. Atoms* **226**, 637–643 (2004).
3. Kokkoris, M. *et al.* A detailed study of the $^{12}\text{C}(d, p0) ^{13}\text{C}$ reaction at detector angles between 135° and 170° , for the energy range $E_{\text{lab}} = 900\text{--}2000$ keV. *Nucl. Instruments Methods Phys. Res. Sect. B: Beam Interactions with Mater. Atoms* **249**, 77–80 (2006).
4. Lanford, W. *et al.* Nuclear reaction analysis for h, li, be, b, c, n, o and f with an rbs check. *Nucl. Instruments Methods Phys. Res. Sect. B: Beam Interactions with Mater. Atoms* **371**, 211–215 (2016).
5. Verma, H. R. *Atomic and nuclear analytical methods* (Springer, 2007).
6. Kokkoris, M. Nuclear reaction analysis (nra) and particle-induced gamma-ray emission (pige). *Charact. Mater.* 1–18 (2002).
7. Rafi-kheiri, H., Kakuee, O. & Lamehi-Rachti, M. Measurements of the $^{24}\text{Mg}(d, p0, 1, 2, 3, 4)$ and $^{nat}\text{Mg}(d, d0)$ reactions cross sections in the energy range of 1.2–2 meV for nra and ebs applications. *Nucl. Instruments Methods Phys. Res. Sect. B: Beam Interactions with Mater. Atoms* **373**, 63–69 (2016).
8. Amsel, G. Spectroscopie par détecteurs à semiconducteur des réactions nucléaires $^{16}\text{O} + d$, $^{18}\text{O} + p$. In *Annales de Physique*, vol. 13, 297–344 (1964).
9. Kokkoris, M. *et al.* Study of selected differential cross-sections of the $^{28}\text{Si}(d, p0, p1, p2, p3)$ reactions for nra purposes. *Nucl. Instruments Methods Phys. Res. Sect. B: Beam Interactions with Mater. Atoms* **267**, 1744–1747 (2009).
10. Gurbich, A. & Molodtsov, S. Measurement of (d, p) and (d, α) differential cross-sections for ^{14}N . *Nucl. Instruments Methods Phys. Res. Sect. B: Beam Interactions with Mater. Atoms* **266**, 1206–1208 (2008).
11. Mateus, R., Fonseca, M., Jesus, A., Luís, H. & Ribeiro, J. Pige analysis and profiling of aluminium. *Nucl. Instruments Methods Phys. Res. Sect. B: Beam Interactions with Mater. Atoms* **266**, 1490–1492 (2008).
12. Healy, M., Pidduck, A., Dollinger, G., Gorgens, L. & Bergmaier, A. Ion beam analysis of aluminium in thin layers. *Nucl. Instruments Methods Phys. Res. Sect. B: Beam Interactions with Mater. Atoms* **190**, 630–635 (2002).
13. Pellegrino, S., Beck, L., Trouslard, P. & Trocellier, P. Differential cross-sections for nuclear reactions on al and si induced by deuterons at low energy (1–2 meV). *Nucl. Instruments Methods Phys. Res. Sect. B: Beam Interactions with Mater. Atoms* **266**, 2268–2272 (2008).
14. Corleo, G. & Sambataro, S. Differential absolute cross-section for the nuclear reactions $^{27}\text{Al}(d, p) ^{28}\text{Al}$ and $^{27}\text{Al}(d, \alpha) ^{25}\text{Mg}$ at $\theta_{\text{lab}} = 90^\circ$. *Il Nuovo Cimento B (1965-1970)* **56**, 83–88 (1968).
15. Corleo, G., Pappalardo, G. & Rubbino, A. Analysis of nuclear reactions with the ^{29}Si as intermediate system. *Il Nuovo Cimento B (1965-1970)* **52**, 248–250 (1967).

16. Lin, C. & Lin, E. The reaction $^{27}\text{Al}(d, p)^{28}\text{Al}$ in the energy range of the deuteron from 2.0 meV to 3.0 meV. *Il Nuovo Cimento A (1965-1970)* **66**, 336–342 (1970).
17. Holz, K., Lietard, J. & Somoza, M. High-power 365 nm uv led mercury arc lamp replacement for photochemistry and chemical photolithography. *ACS sustainable chemistry & engineering* **5**, 828–834 (2017).
18. Dalmau, R. *et al.* Growth and characterization of aln and algan epitaxial films on aln single crystal substrates. *J. The Electrochem. Soc.* **158**, H530 (2011).
19. Redondo-Cubero, A. *et al.* Aluminium incorporation in alxga1-xn/gan heterostructures: A comparative study by ion beam analysis and x-ray diffraction. *Thin Solid Films* **516**, 8447–8452 (2008).
20. Zhang, J. *et al.* A study of the degree of relaxation of algan epilayers on gan template. *J. crystal growth* **270**, 289–294 (2004).
21. Gadioli, E., Iori, I., Mangialaio, M. & Pappalardo, G. Study of the $^{27}\text{Al}(d, \alpha)^{25}\text{Mg}$ and $^{27}\text{Al}(d, p)^{28}\text{Al}$ nuclear reactions at 2 meV deuteron energy. *Il Nuovo Cimento (1955-1965)* **38**, 1105–1132 (1965).
22. Corti, M., Marcazzan, G., Colli, L. M. & Milazzo, M. Direct effect and evaporation mechanism in $^{27}\text{Al}(d, p)^{28}\text{Al}$ and $^{27}\text{Al}(d, \alpha)^{25}\text{Mg}$ reactions. *Nucl. Phys.* **77**, 625–640 (1966).
23. Osman, A. & Din, G. The (d, p) reactions below 3.0 meV. *Annalen der Physik* **491**, 64–80 (1979).
24. Kakuee, O., Fathollahi, V. & Lamehi-Rachti, M. Development of a versatile user-friendly iba experimental chamber. *Nucl. Instruments Methods Phys. Res. Sect. B: Beam Interactions with Mater. Atoms* **371**, 156–160 (2016).
25. Jokar, A., Kakuee, O. & Lamehi-Rachti, M. Differential cross sections measurement of $^{31}\text{P}(p, p\gamma)^{31}\text{P}$ reaction for pipeapplications. *Nucl. Instruments Methods Phys. Res. Sect. B: Beam Interactions with Mater. Atoms* **383**, 152–155 (2016).
26. Amsel, G. & Davies, J. Precision standard reference targets for microanalysis by nuclear reactions. *Nucl. Instruments Methods Phys. Res.* **218**, 177–182 (1983).
27. Morrall, P. The target preparation laboratory at daresbury. *Nucl. Instruments Methods Phys. Res. Sect. A: Accel. Spectrometers, Detect. Assoc. Equip.* **590**, 118–121 (2008).
28. Rafi-kheiri, H., Kakuee, O. & Lamehi-Rachti, M. Differential cross section measurement of the $^{nat}\text{O}(d, d^0)$ reaction at energies and angles relevant to EBS. *Nucl. Instruments Methods Phys. Res. Sect. B: Beam Interactions with Mater. Atoms* **373**, 40–43 (2016).
29. Rubehn, T., Wozniak, G., Phair, L., Moretto, L. & Yu, K. M. Characterization of nuclear physics targets using rutherford backscattering and particle induced x-ray emission. *Nucl. Instruments Methods Phys. Res. Sect. A: Accel. Spectrometers, Detect. Assoc. Equip.* **387**, 328–332 (1997).
30. Mayer, M. Simnra, a simulation program for the analysis of nra, rbs and erda. In *AIP conference proceedings*, vol. 475, 541–544 (American Institute of Physics, 1999).
31. Amsel, G., d'Artemare, E. & Girard, E. A simple, digitally controlled, automatic, hysteresis free, high precision energy scanning system for van de graaff type accelerators: Part i: Principle, results and applications. *Nucl. Instruments Methods Phys. Res.* **205**, 5–26 (1983).
32. Amsel, G. *et al.* Narrow nuclear resonance position or cross section shape measurements with a high precision computer controlled beam energy scanning system. *Nucl. Instruments Methods Phys. Res. Sect. B: Beam Interactions with Mater. Atoms* **136**, 545–550 (1998).
33. Vickridge, I. & Amsel, G. Spaces: A pc implementation of the stochastic theory of energy loss for narrow-resonance depth profiling. *Nucl. Instruments Methods Phys. Res. Sect. B: Beam Interactions with Mater. Atoms* **45**, 6–11 (1990).
34. Abuzeid, M. *et al.* The reaction $^{27}\text{Al}(d, \alpha)^{25}\text{Mg}$ in the deuteron energy range 1.5–2.6 meV. *Nucl. Phys.* **54**, 315–320 (1964).
35. Abriola, D. *et al.* Development of a reference database for ion beam analysis and future perspectives. *Nucl. Instruments Methods Phys. Res. Sect. B: Beam Interactions with Mater. Atoms* **269**, 2972–2978 (2011).
36. Oppenheim, A. V. Alan S. Willsky, Ian T. Young. *Signals Syst. Englewood Cliffs, NJ: Prentice-Hall, Inc* (1983).
37. Devore, J. L. *Probability and Statistics for Engineering and the Sciences* (Cengage Learning, 2015).
38. Chiari, M. & Dimitriou, P. Technical meeting on benchmarking experiments for ion beam analysis. summary report. *Tech. Rep., International Atomic Energy Agency* (2016).
39. Kokkoris, M. *et al.* Benchmarking the evaluated proton differential cross sections suitable for the ebs analysis of ^{nat}Si and ^{16}O . *Nucl. Instruments Methods Phys. Res. Sect. B: Beam Interactions with Mater. Atoms* **405**, 50–60 (2017).

Table 1. The coefficients and Goodness of fitting for final fitting.

	$^{27}\text{Al}(\text{d},\alpha_0)^{25}\text{Mg}$	$^{27}\text{Al}(\text{d},\alpha_1)^{25}\text{Mg}$	$^{27}\text{Al}(\text{d},\alpha_2)^{25}\text{Mg}$	$^{27}\text{Al}(\text{d},\alpha_3)^{25}\text{Mg}$	$^{27}\text{Al}(\text{d},\alpha_4)^{25}\text{Mg}$	$^{27}\text{Al}(\text{d},\text{p}_{0+1})^{25}\text{Al}$	$^{27}\text{Al}(\text{d},\text{p}_{2+3})^{25}\text{Al}$	$^{27}\text{Al}(\text{d},\text{p}_4)^{25}\text{Al}$	$^{27}\text{Al}(\text{d},\text{p}_{5+6})^{25}\text{Al}$
a0	0.3102	0.1135	0.2474	0.3491	0.2877	0.7530	0.3259	0.1097	0.2070
a1	-0.0212	-0.0186	-0.0270	-0.0583	-0.0268	0.1395	0.0736	0.0328	0.0591
a2	-0.0601	-0.0182	-0.0077	-0.0181	0.0684	-0.1852	-0.0587	-0.0060	-0.0334
a3	-0.0442	-0.0056	-0.0422	-0.0582	-0.0113	0.0210	-0.0086	0.0120	-0.0027
a4	-0.0247	-0.0133	-0.0319	-0.0536	0.0087	0.0258	0.0107	0.0026	0.0033
a5	-0.0155	0.0034	-0.0113	0.0047	0.0016	-0.0588	-0.0198	-0.0068	-0.0178
a6	-0.0039	-0.0069	-0.0059	0.0019	-0.0090	0.0617	0.0117	0.0059	0.0036
a7	0.0126	0.0047	0.0033	-0.0135	0.0116	-0.0078	0.0052	-0.0014	0.0004
a8	0.0001	-0.0002	0.0015	0.0020	-0.0061	-0.0170	-0.0006	-0.0041	-0.0056
a9	0.0019	0.0009	0.0069	0.0052	-0.0021	0.0461	0.0059	0.0037	-0.0009
a10	0.0043	0.0011	0.0050	0.0127	0.0027	-0.0069	-0.0074	-0.0025	-0.0033
a11	0.0069	-0.0005	-0.0013	0.0100	-0.0010	-0.0170	0.0007	-0.0018	-0.0031
a12	0.0021	-0.0002	0.0020	0.0017	0.0033	0.0183	0.0082	0.0022	0.0039
a13	0.0000	0.0008	-0.0023	0.0056	0.0000	-0.0098	-0.0018	-0.0031	-0.0014
a14	-0.0010	-0.0005	-0.0015	-0.0010	-0.0022	-0.0032	-0.0011	0.0002	-0.0023
a15	-0.0038	-0.0018	-0.0029	-0.0021	0.0038	0.0082	0.0038	0.0031	0.0020
a16	-0.0049	-0.0005	-0.0041	-0.0063	-0.0016	-0.0101	-0.0004	-0.0008	-0.0003
a17	-0.0042	-0.0013	-0.0036	-0.0073	-0.0007	0.0072	0.0024	0.0002	0.0011
a18	-0.0040	-0.0013	-0.0039	-0.0036	0.0026	0.0050	-0.0016	0.0003	0.0010
a19	-0.0024	-0.0008	-0.0022	-0.0034	-0.0030	0.0006	0.0005	0.0014	0.0005
a20	-0.0002	0.0003	-0.0013	-0.0020	0.0022	0.0023	0.0009	0.0012	-0.0005
b1									
b1	-0.0945	-0.0291	-0.0502	-0.1104	0.0425	0.2519	0.0933	0.0164	0.0501
b2	-0.0442	-0.0097	-0.0099	-0.0662	-0.0309	0.0331	0.0389	-0.0108	0.0241
b3	0.0088	0.0164	-0.0263	-0.0033	-0.0160	-0.1105	-0.0390	-0.0272	-0.0113
b4	0.0310	-0.0022	0.0238	0.0313	0.0179	0.0541	0.0216	-0.0001	0.0219
b5	0.0098	0.0075	0.0161	0.0312	-0.0160	-0.0433	-0.0028	-0.0055	0.0041
b6	0.0208	0.0009	0.0211	0.0000	-0.0014	-0.0438	-0.0139	0.0006	-0.0099
b7	0.0073	0.0058	0.0126	0.0169	0.0120	0.0460	-0.0006	0.0081	0.0049
b8	0.0029	0.0025	0.0082	0.0093	-0.0113	-0.0247	-0.0137	-0.0043	-0.0023
b9	0.0058	0.0008	0.0083	0.0130	0.0047	-0.0094	-0.0005	0.0017	-0.0015
b10	0.0037	-0.0003	-0.0022	0.0028	-0.0020	0.0257	0.0002	0.0028	0.0020
b11	-0.0031	-0.0011	-0.0033	-0.0082	-0.0015	-0.0204	-0.0086	-0.0036	-0.0032
b12	-0.0043	0.0011	-0.0029	-0.0040	0.0029	-0.0006	0.0016	0.0011	0.0000
b13	-0.0055	-0.0017	-0.0059	-0.0088	-0.0048	0.0176	0.0050	0.0014	0.0021
b14	-0.0052	-0.0017	-0.0049	-0.0072	0.0013	-0.0103	-0.0049	-0.0024	-0.0021
b15	-0.0041	-0.0015	-0.0053	-0.0062	0.0023	0.0020	0.0013	0.0016	0.0001
b16	-0.0022	-0.0002	-0.0007	-0.0040	-0.0041	0.0034	0.0003	0.0020	0.0018
b17	-0.0008	-0.0010	-0.0005	0.0008	0.0045	-0.0070	0.0002	-0.0008	-0.0015
b18	0.0014	0.0002	0.0017	0.0017	0.0002	0.0064	0.0033	0.0003	0.0002
b19	0.0018	0.0012	0.0022	0.0029	-0.0026	-0.0009	-0.0012	-0.0006	0.0010
b20	0.0022	0.0002	0.0004	0.0020	0.0033	0.0014	0.0021	0.0009	0.0007
$\omega=2\pi/T$									
ω	0.0092	0.0092	0.0092	0.0092	0.0113	0.0071	0.0071	0.0071	0.0071
Goodness of Fitting									
R²	0.9767	0.9681	0.949	0.965	0.9139	0.9657	0.9699	0.947	0.9751

Figures:

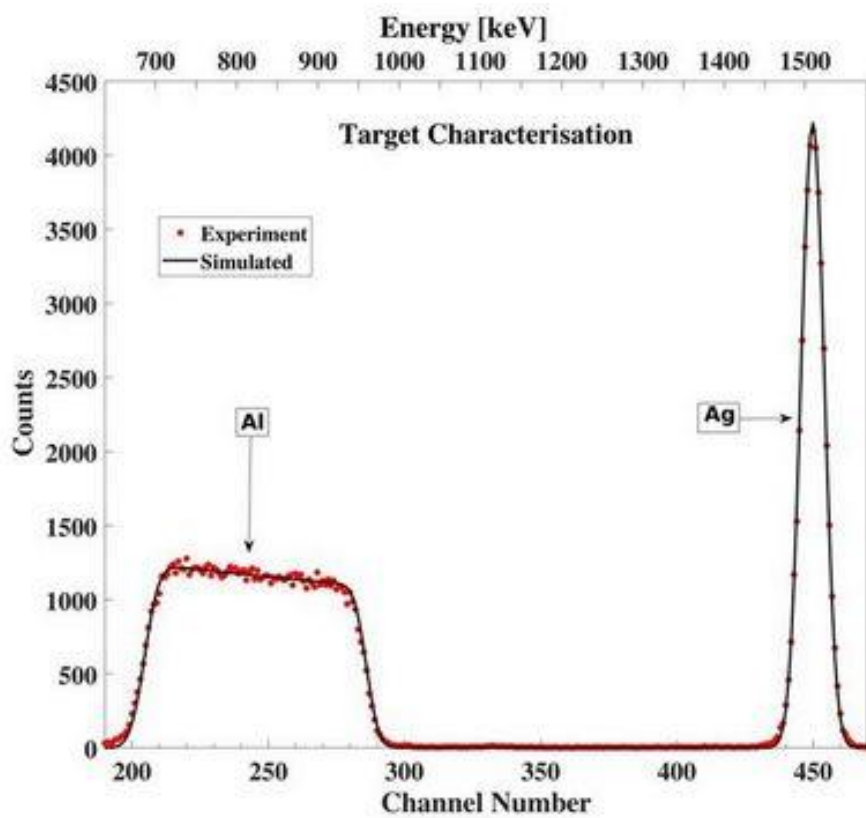
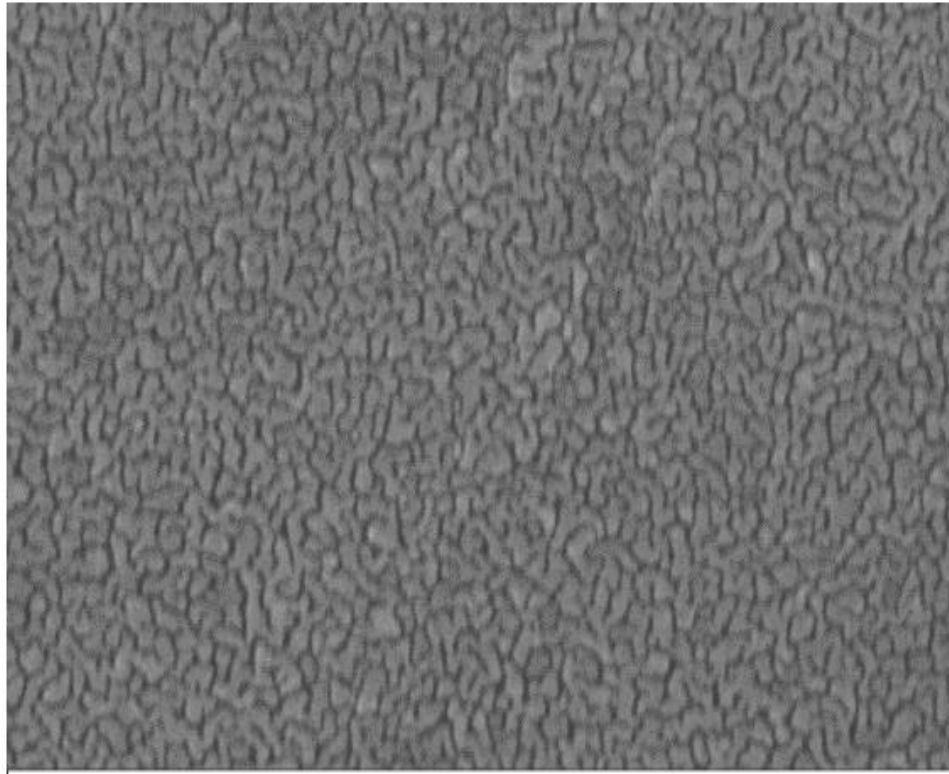


Fig.1. Typical simulated and measured RBS spectra from a thin Al/Ag target obtained at scattering angle 150° and $E_\alpha = 1.8$ MeV.




100 nm

Mag = 80.54 KX
WD = 9.8 mm
Stage at T = 0.0 °

Signal A = InLens
EHT = 20.00 kV
Date : 18 Dec 2020



Fig. 2. SEM images of the surface of from Au/Al target

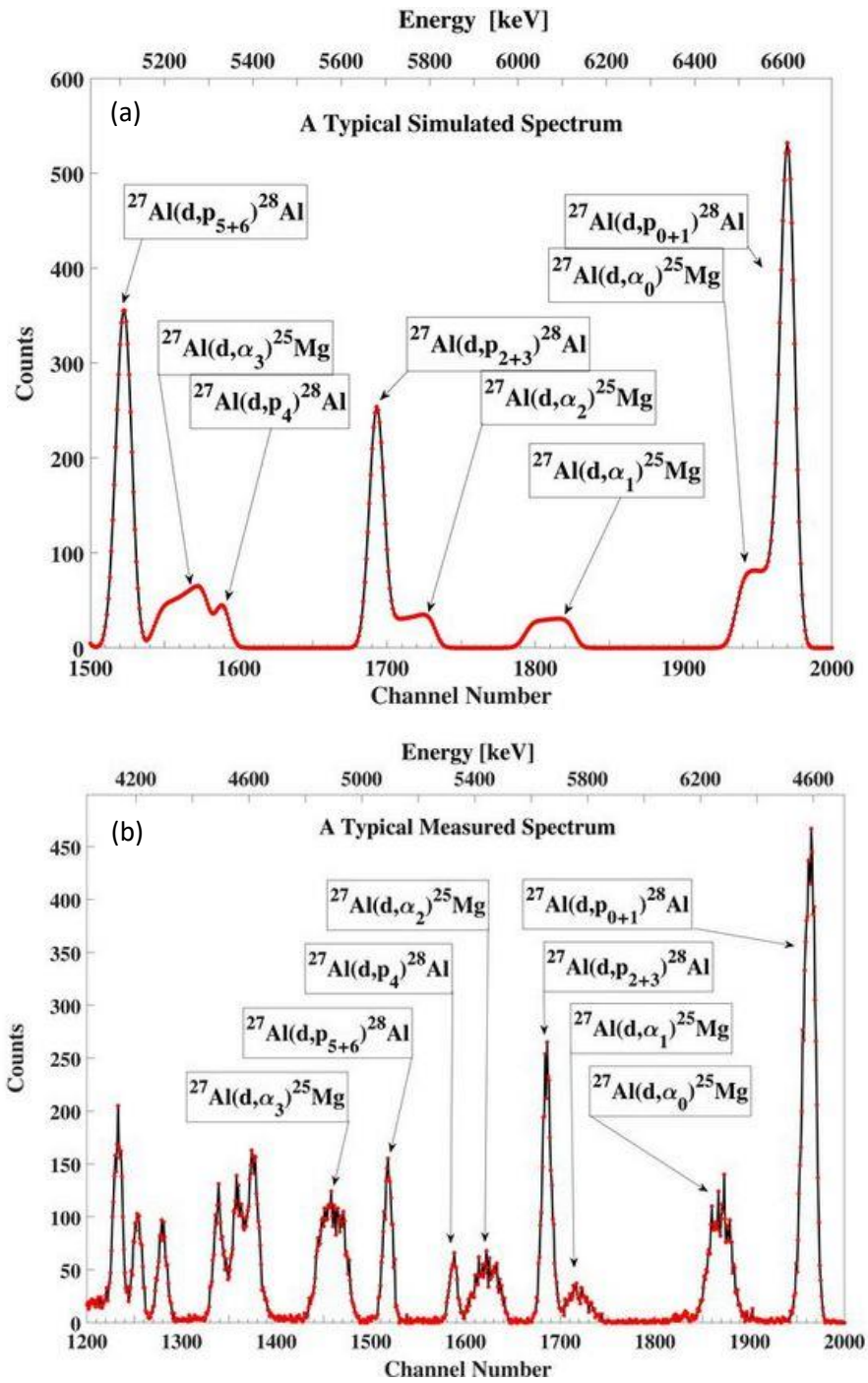


Fig. 3. (a) The simulated spectrum without mylar and (b) the typical measured spectrum in experimental work with $4\mu\text{m}$ mylar in front of the particle detector at the detection angle of 150° and for $E_{d,\text{lab}} = 1.8$ MeV at VDGT Lab in Tehran. The interferences between the high energy alpha and proton groups are clearly resolved.

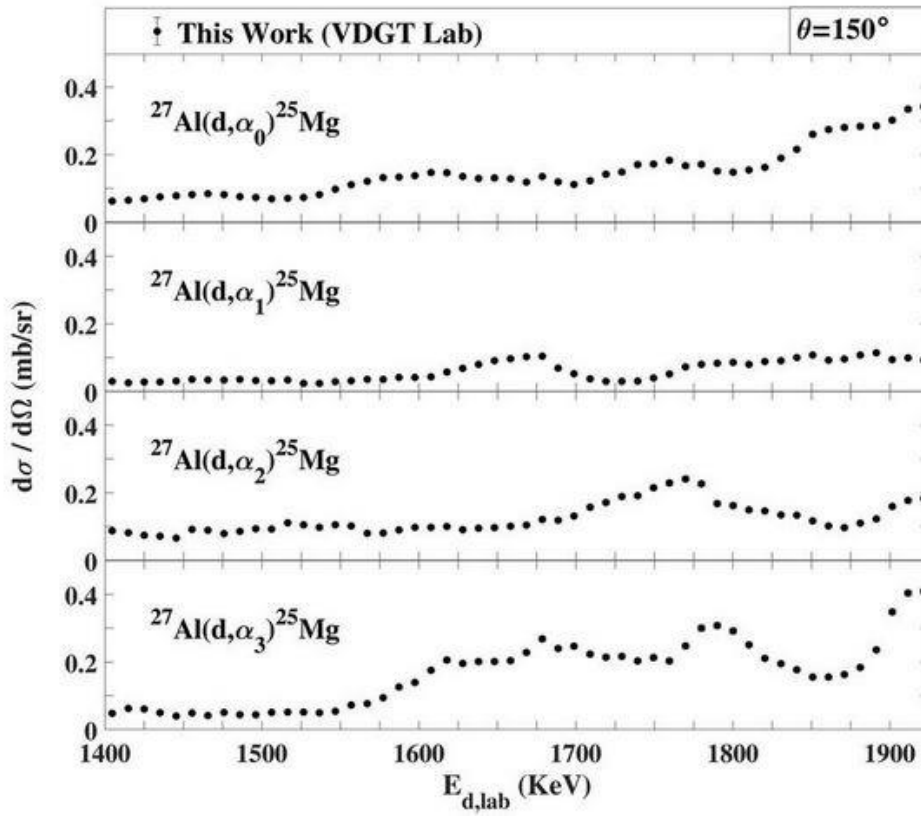


Fig. 4. The excitation functions at scattering angle 150° at VDGTLab in Tehran for the $^{27}\text{Al}(d,\alpha)^{25}\text{Mg}$ reactions. The estimated uncertainties from counting statistics are smaller than the plotted symbols.

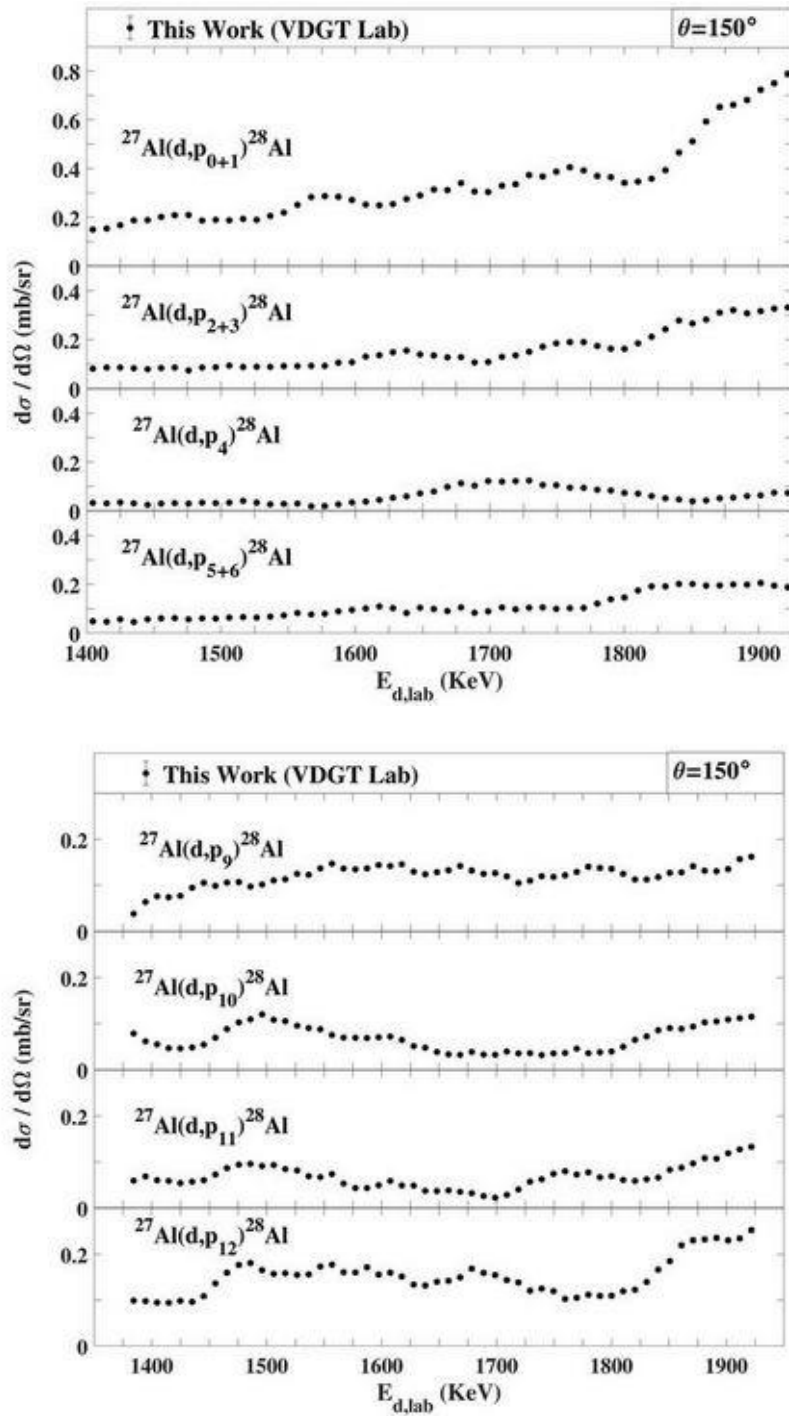


Fig. 5. Differential cross section values for the $^{27}\text{Al}(d,p_{0-12})^{28}\text{Al}$ reactions at scattering angle 150° at VDGTLab in Tehran. The estimated uncertainties from counting statistics are smaller than the plotted symbols.

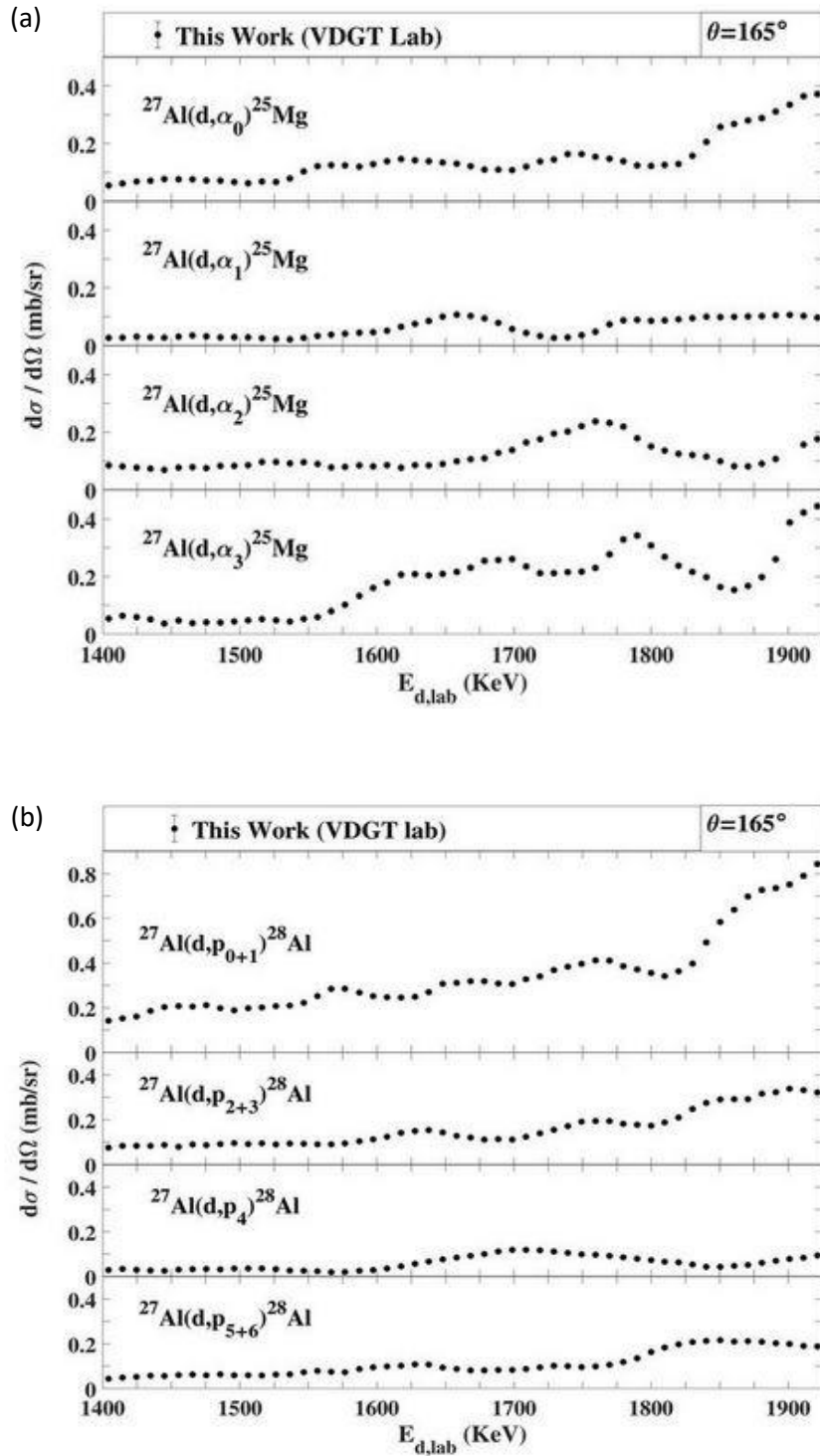


Fig. 6. The differential cross sections at 165° measured at VDGTLab in Tehran for the (a) $^{27}\text{Al}(d, \alpha)^{25}\text{Mg}$ and (b) $^{27}\text{Al}(d, p)^{28}\text{Al}$ reactions. The estimated uncertainties from counting statistics are smaller than the plotted symbols.

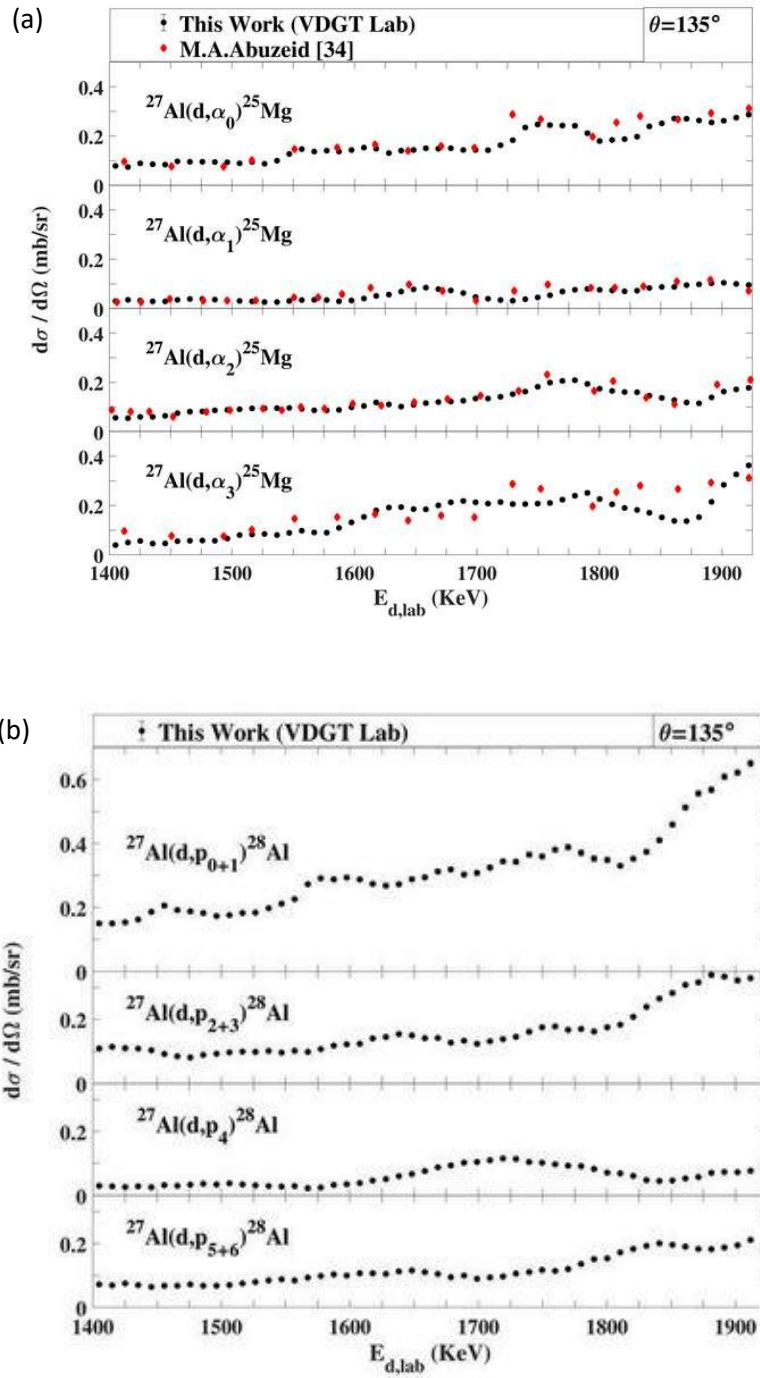


Fig. 7. The differential cross sections measured at 135° at VDGTLab in Tehran for the (a) $^{27}\text{Al}(d,\alpha)^{25}\text{Mg}$ reactions together with the data from [34], and (b) $^{27}\text{Al}(d,p)^{28}\text{Al}$ reactions. The estimated uncertainties from counting statistics are smaller than the plotted symbols.

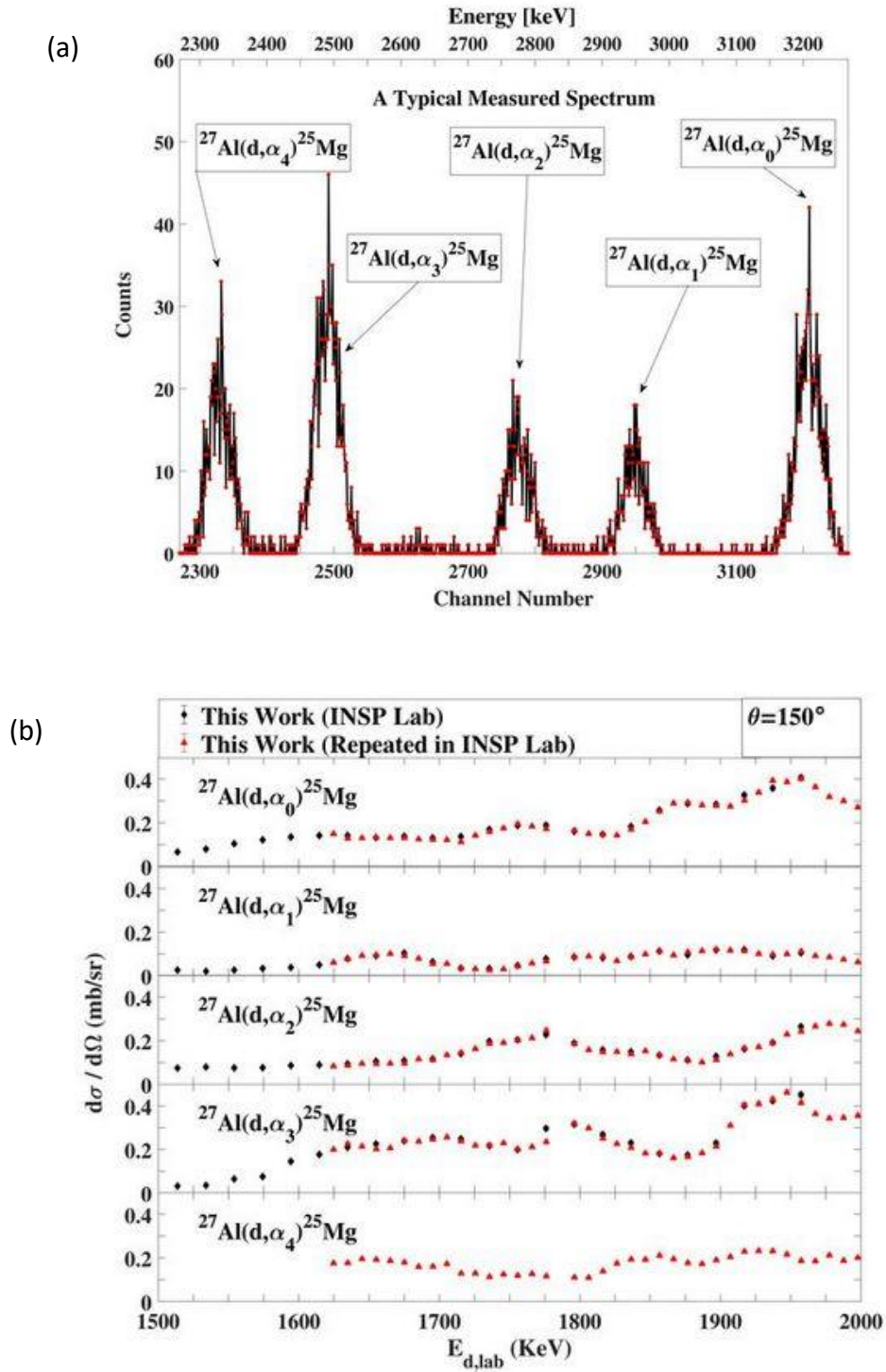


Fig. 8. (a) A typical spectrum of α -particles for the $^{27}\text{Al}(d, \alpha)^{25}\text{Mg}$ reaction, (b) The excitation functions for the $^{27}\text{Al}(d, \alpha)^{25}\text{Mg}$ reaction at scattering angle 150° at INSP Lab in Paris. The estimated uncertainties from counting statistics are smaller than the plotted symbols.

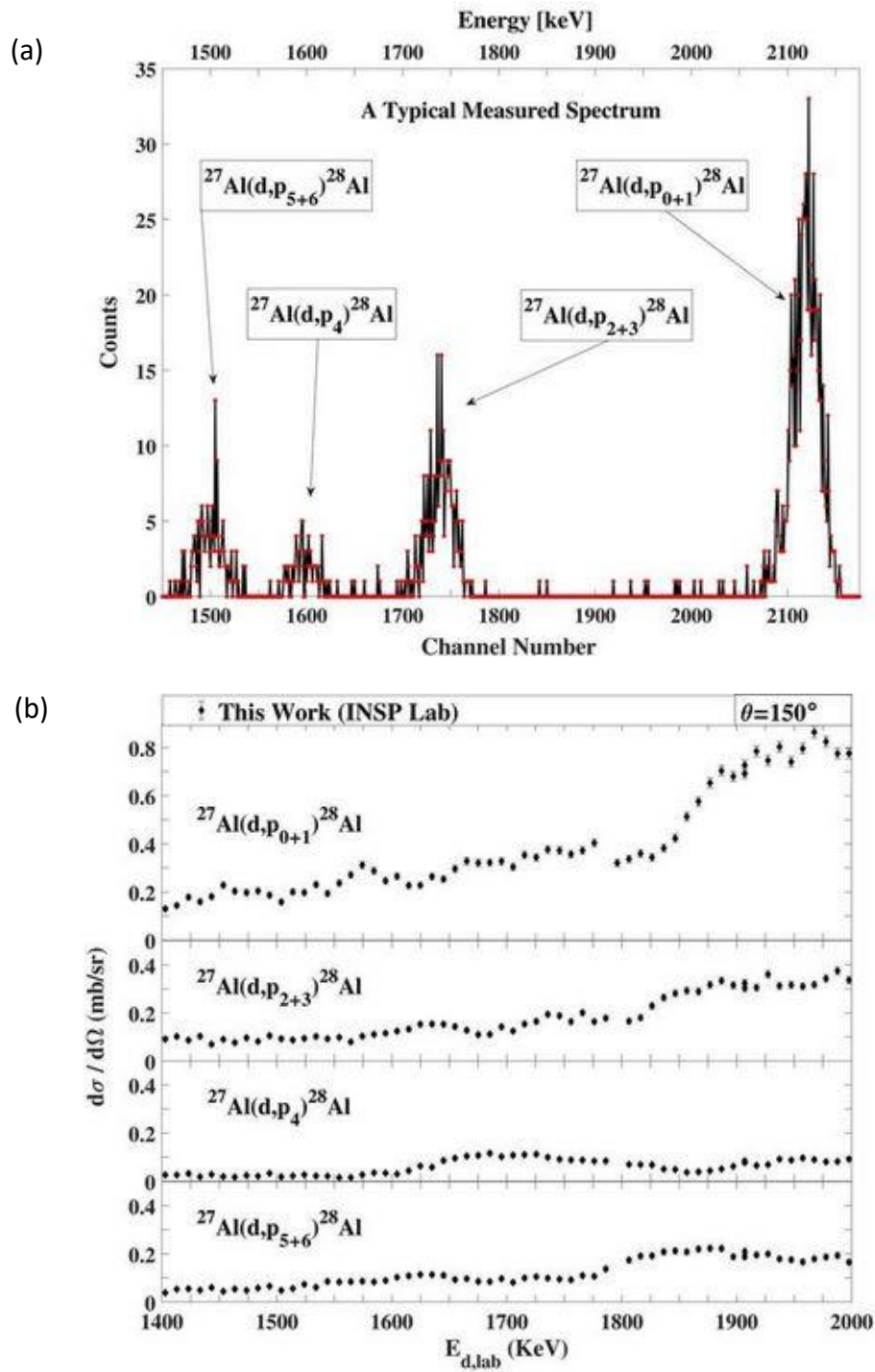


Fig. 9. (a) A typical spectrum of protons for the $^{27}\text{Al}(d,p)^{28}\text{Al}$ reaction. (b) The excitation functions for the $^{27}\text{Al}(d,p)^{28}\text{Al}$ reaction at scattering angle 150° at INSP Lab in Paris. Where not visible, the estimated uncertainties from counting statistics are smaller than the plotted symbols.

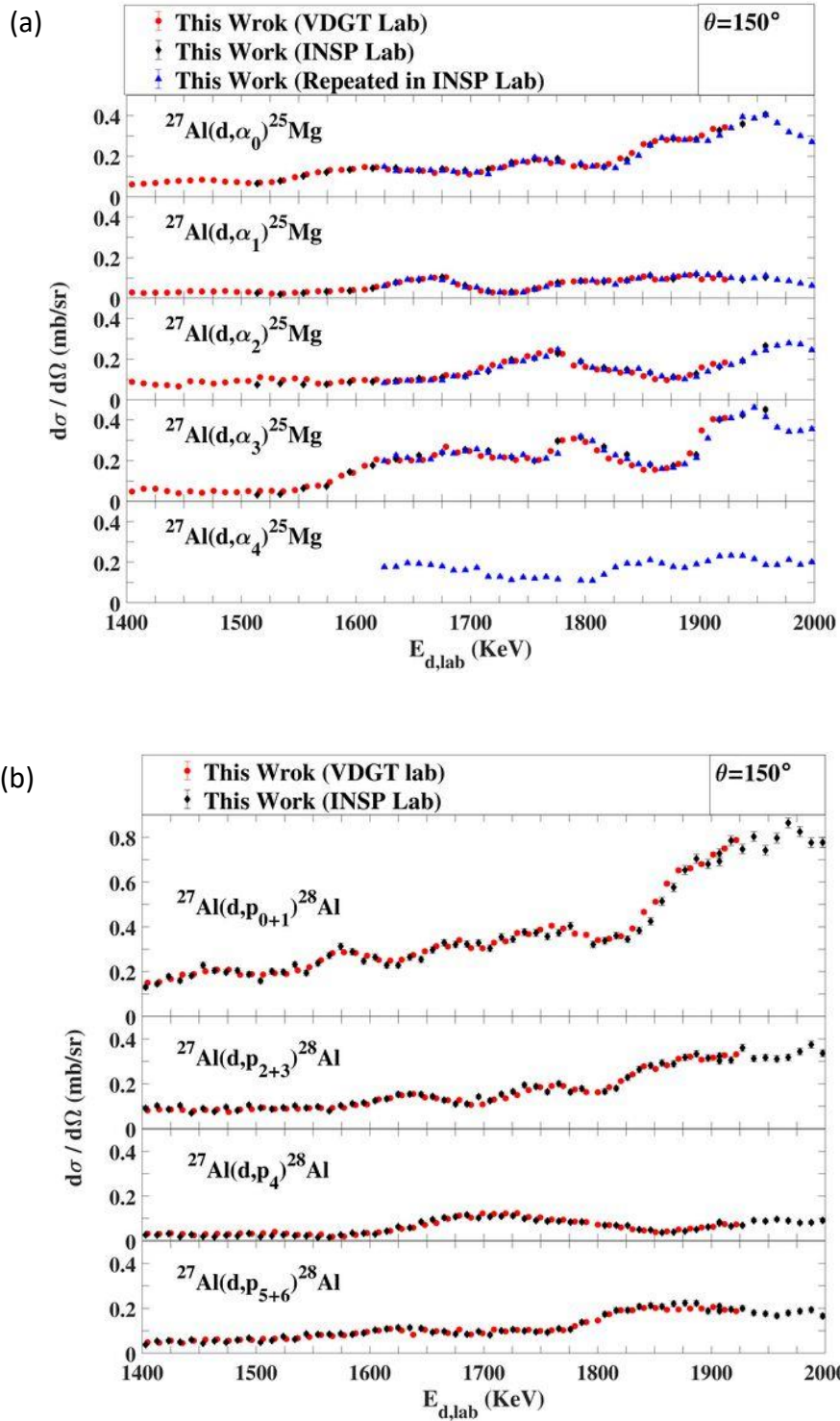


Fig. 10. The comparison between our data from VDGT and from INSP at 150° for the (a) $^{27}\text{Al}(d, \alpha_{0,1,2,3,4})^{25}\text{Mg}$ and (b) $^{27}\text{Al}(d, p_{0+1,2+3,4,5+6})^{28}\text{Al}$ reactions.

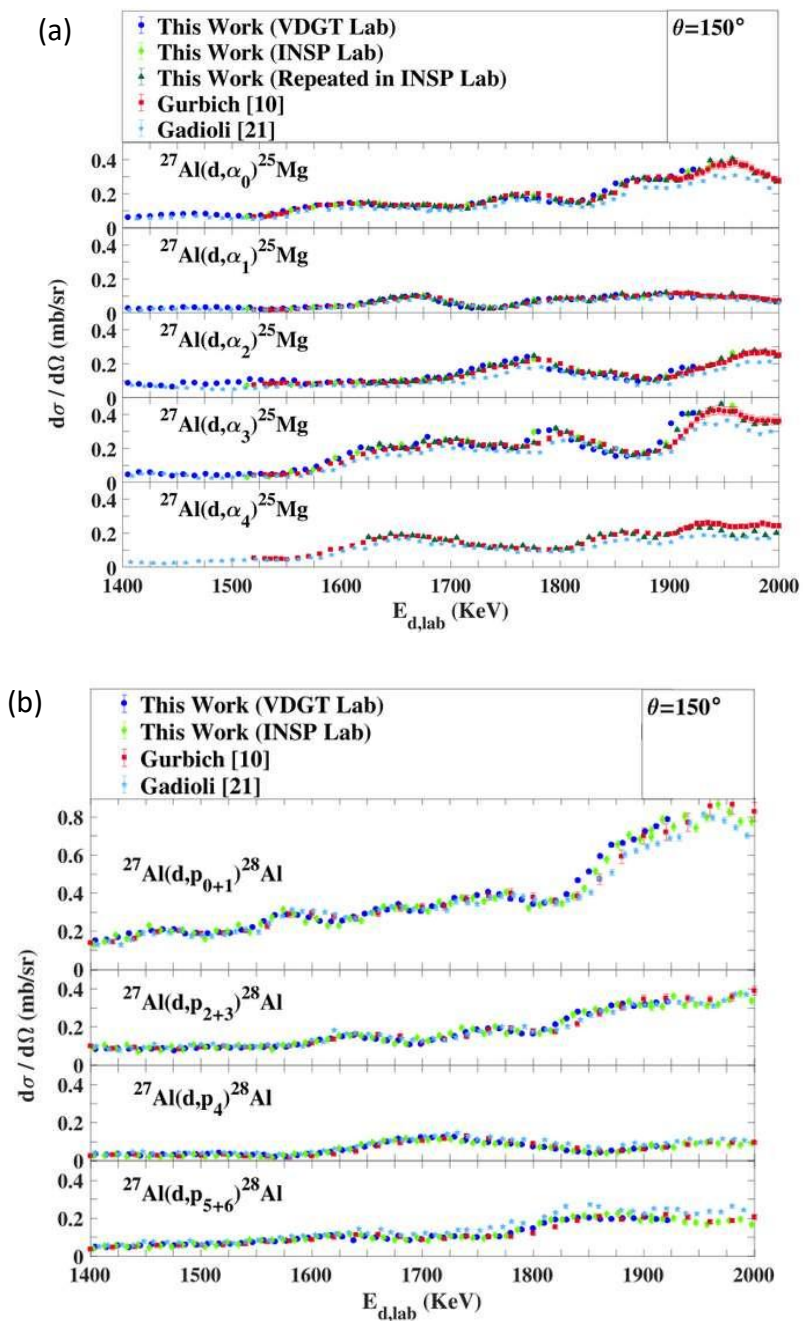


Fig. 11. The comparison of our work with other data at 150° for (a) $^{27}\text{Al}(d, \alpha_{0,1,2,3,4})^{25}\text{Mg}$ and (b) $^{27}\text{Al}(d, p_{0+1,2+3,4,5+6})^{28}\text{Al}$ reactions [10, 21]

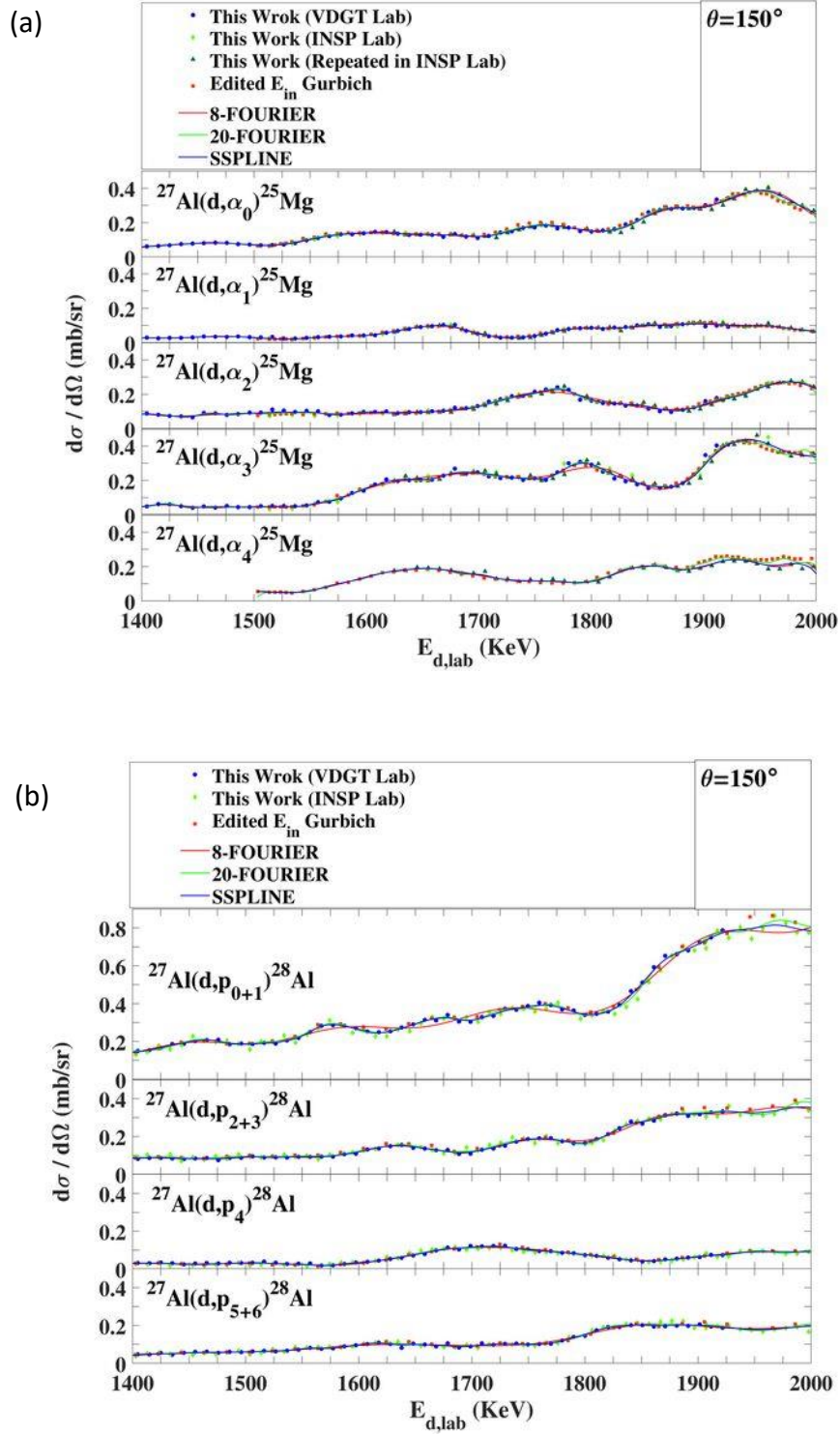


Fig. 12. The comparison of different fitting methods for cross sections at 150° for (a) $^{27}\text{Al}(d, \alpha_{0,1,2,3,4})^{25}\text{Mg}$ and (b) $^{27}\text{Al}(d, p_{0+1,2+3,4,5+6})^{28}\text{Al}$ reactions.

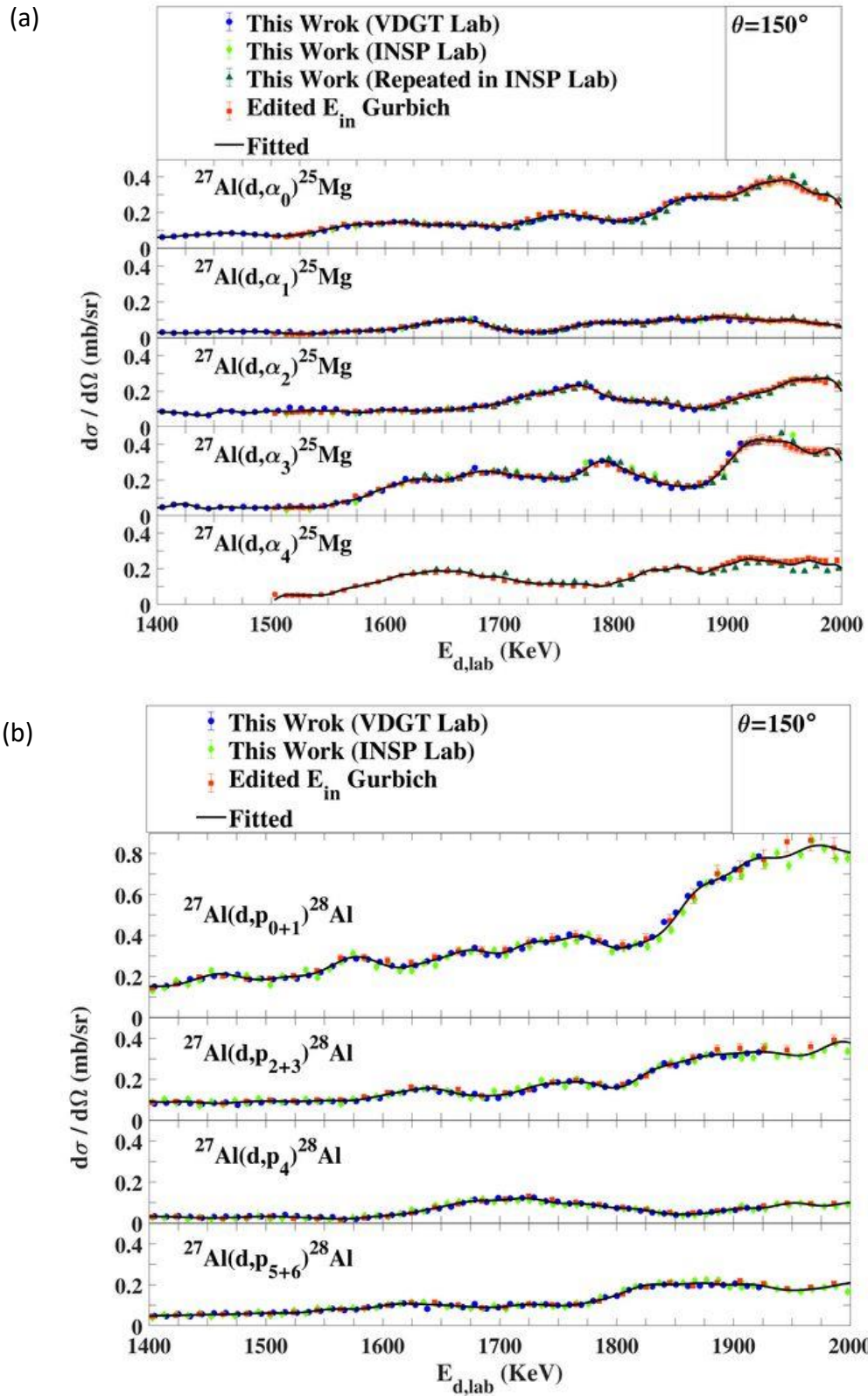


Fig. 13. The fitted data for 150° for (a) $^{27}\text{Al}(d, \alpha_{0,1,2,3,4})^{25}\text{Mg}$ and (b) $^{27}\text{Al}(d, p_{0+1,2+3,4,5+6})^{28}\text{Al}$ reactions.

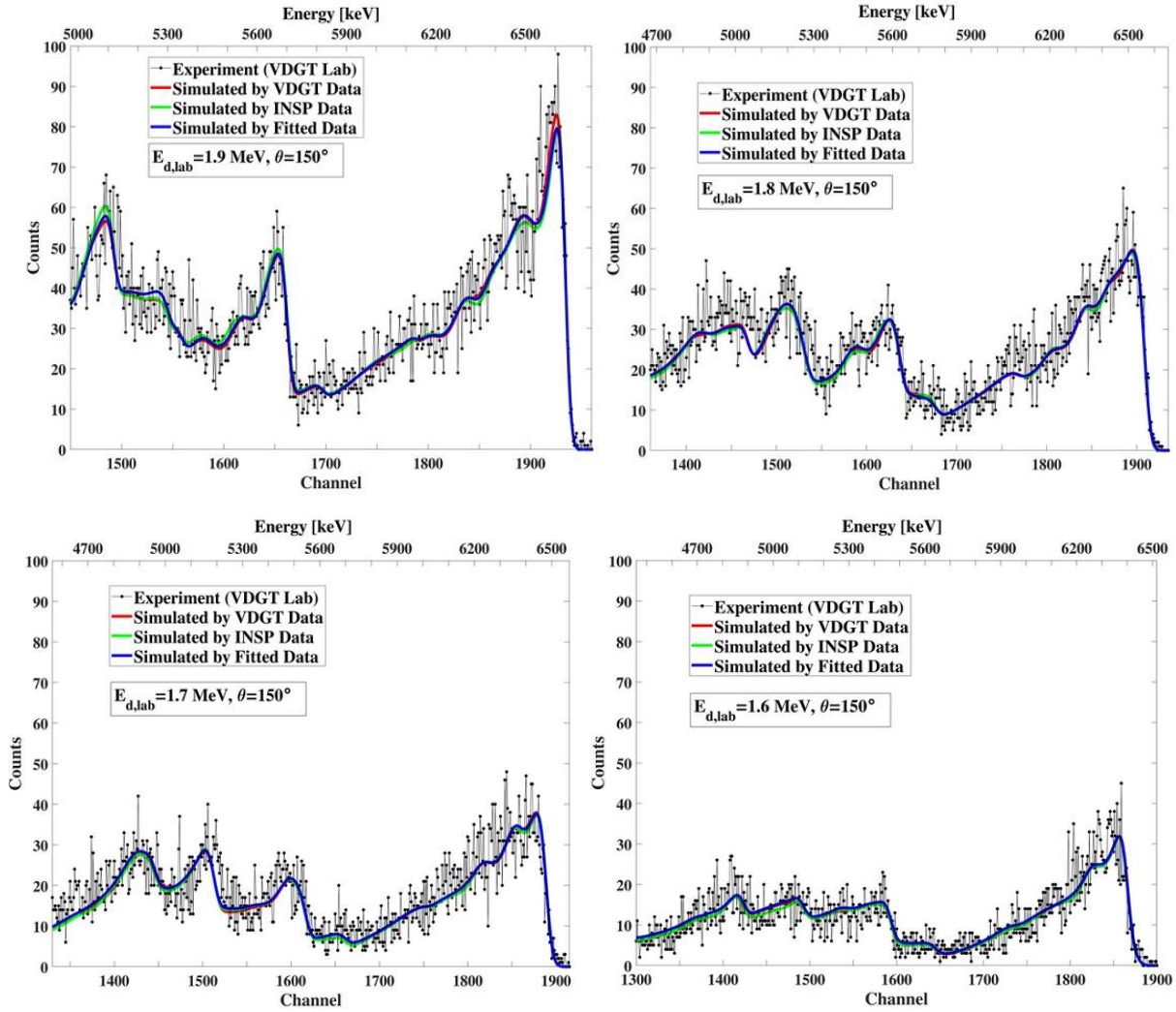


Fig. 14. The benchmarking result at VDG Lab in Tehran with different data sets and different incident deuteron energies at 150° .

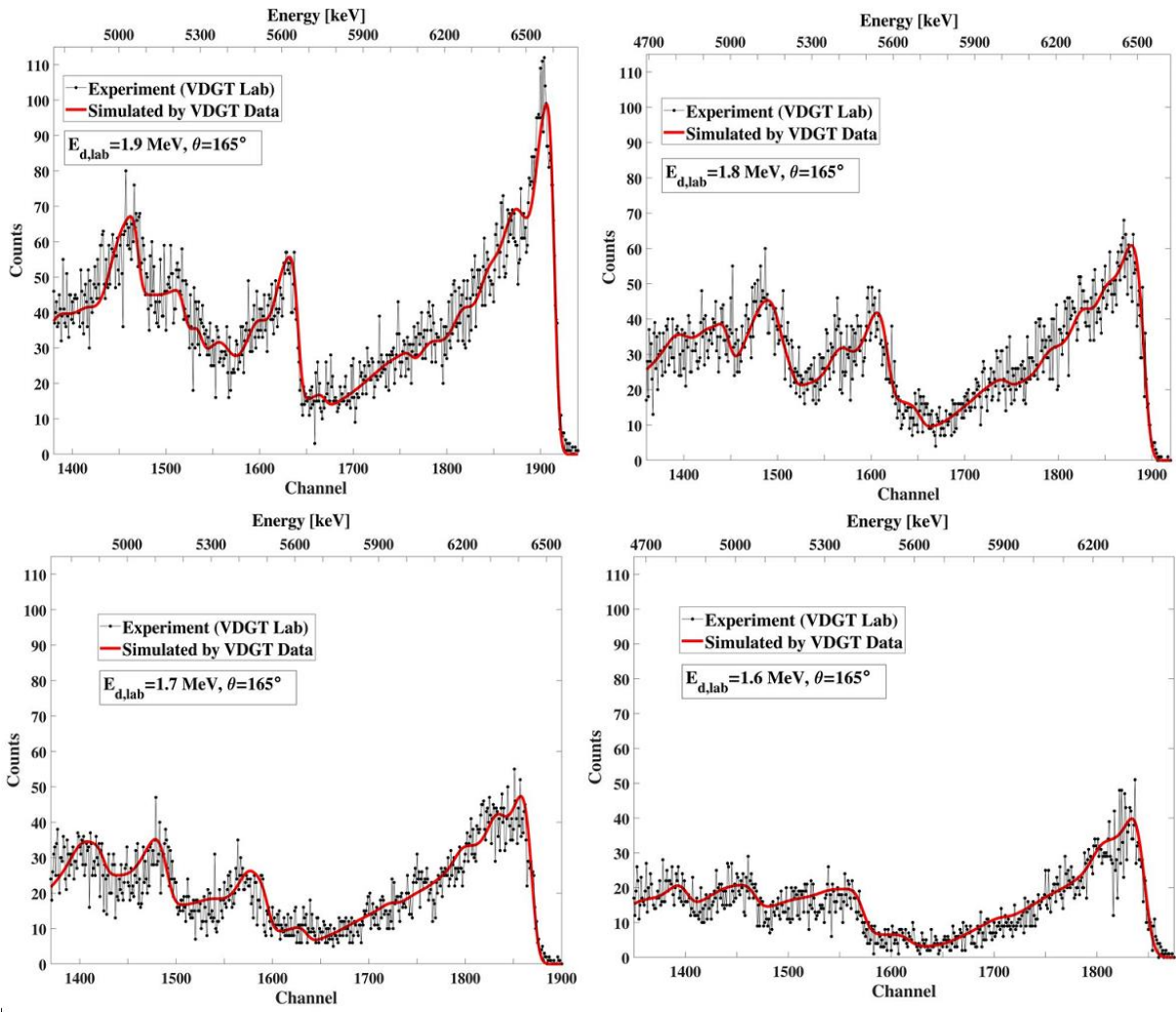


Fig. 15. The benchmarking result at VDGT Lab in Tehran with measured VDGT data at different incident deuteron energies at 165° .

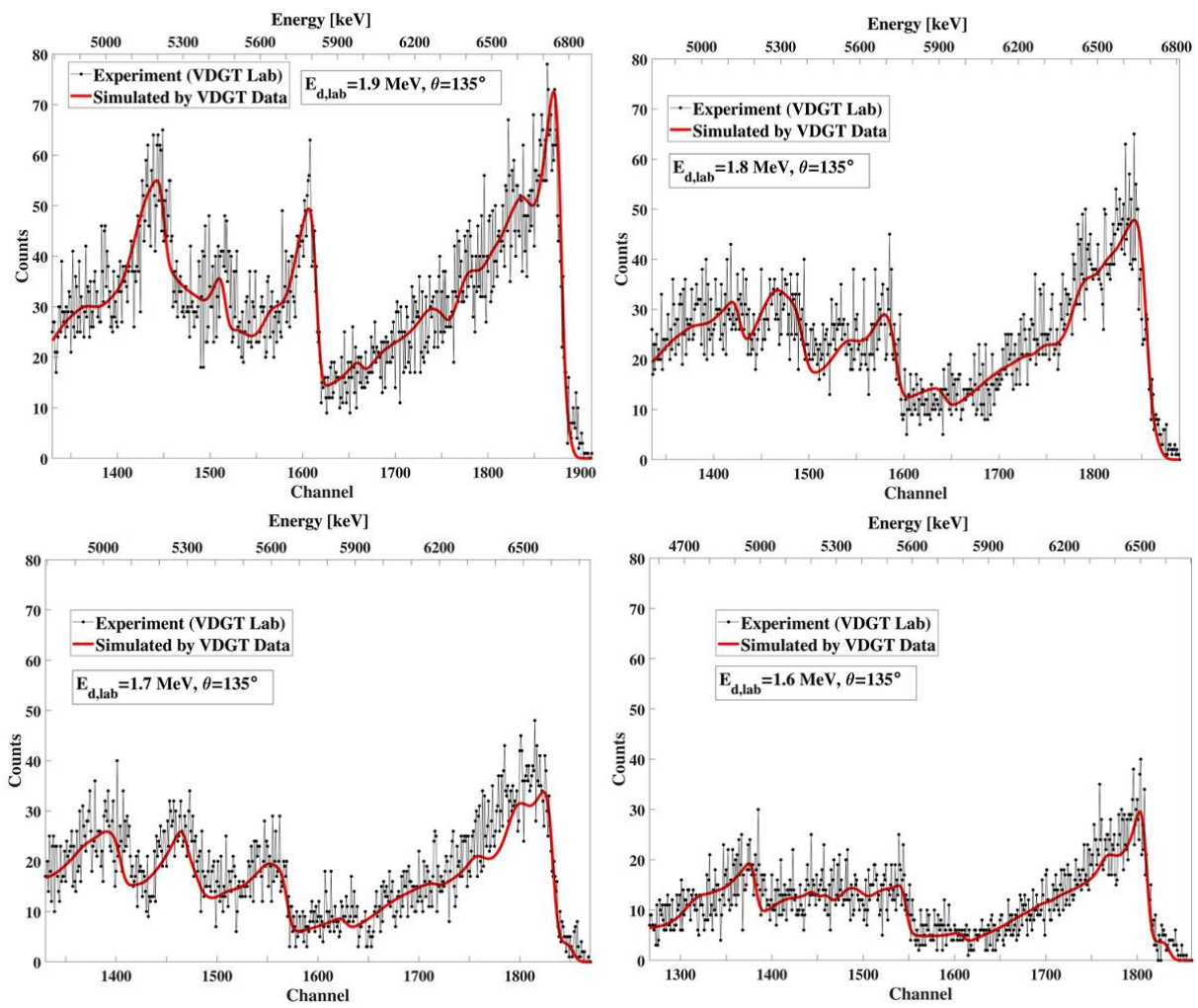


Fig. 16. The benchmarking result at VDGT Lab in Tehran with measured VDGT data with different incident deuteron energies at 135° .

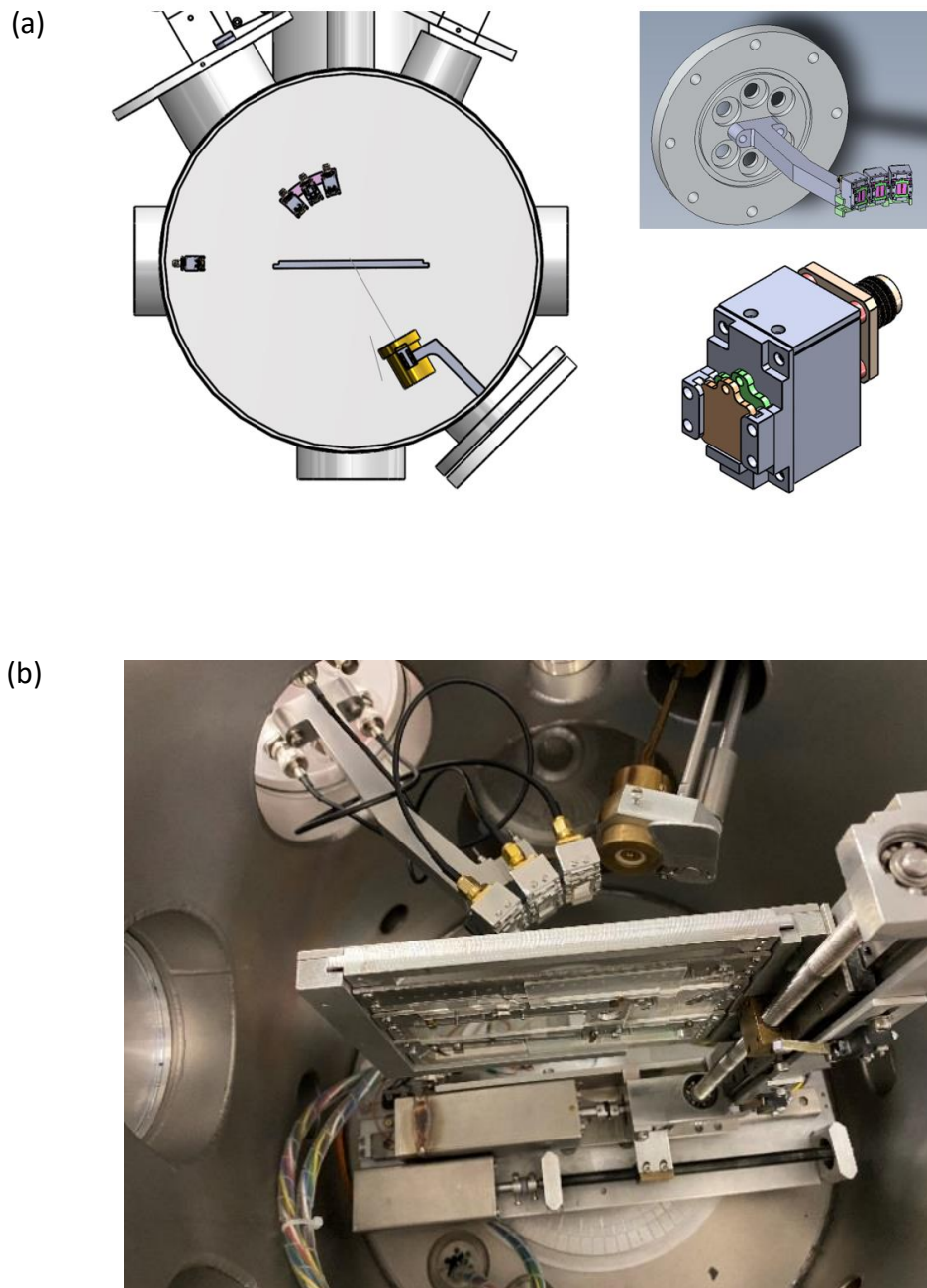


Fig. 17. (a) Simulation of multi-detector holder, (b) Set up of three pin detectors with 100µm mylar in front of the detector.

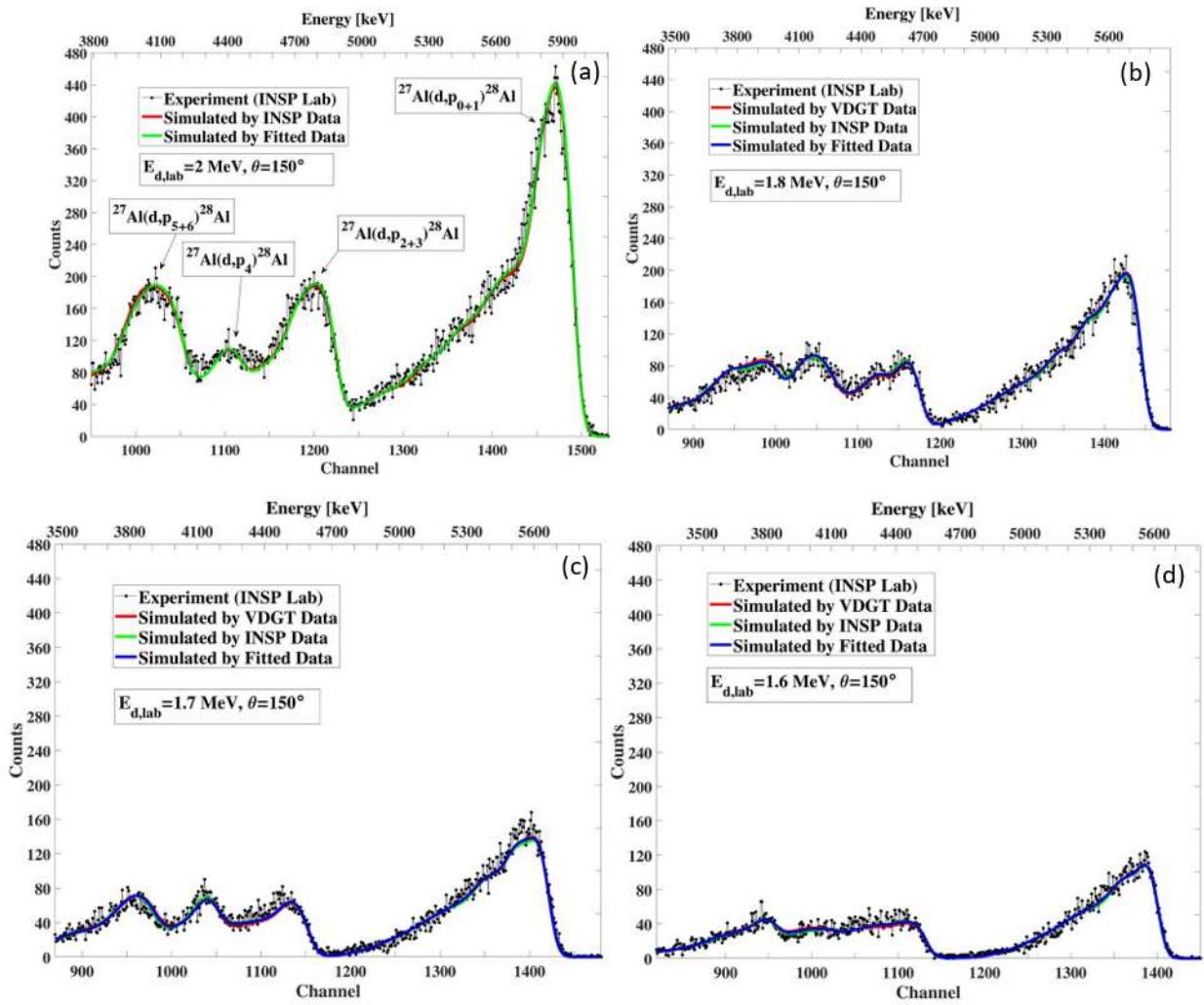


Fig. 18. The benchmarking result at INSP Lab in Paris with different data set at 150° for incident deuteron energies of (a) 2 MeV, (b) 1.8 MeV, (c) 1.7 MeV, (d) 1.6 MeV.

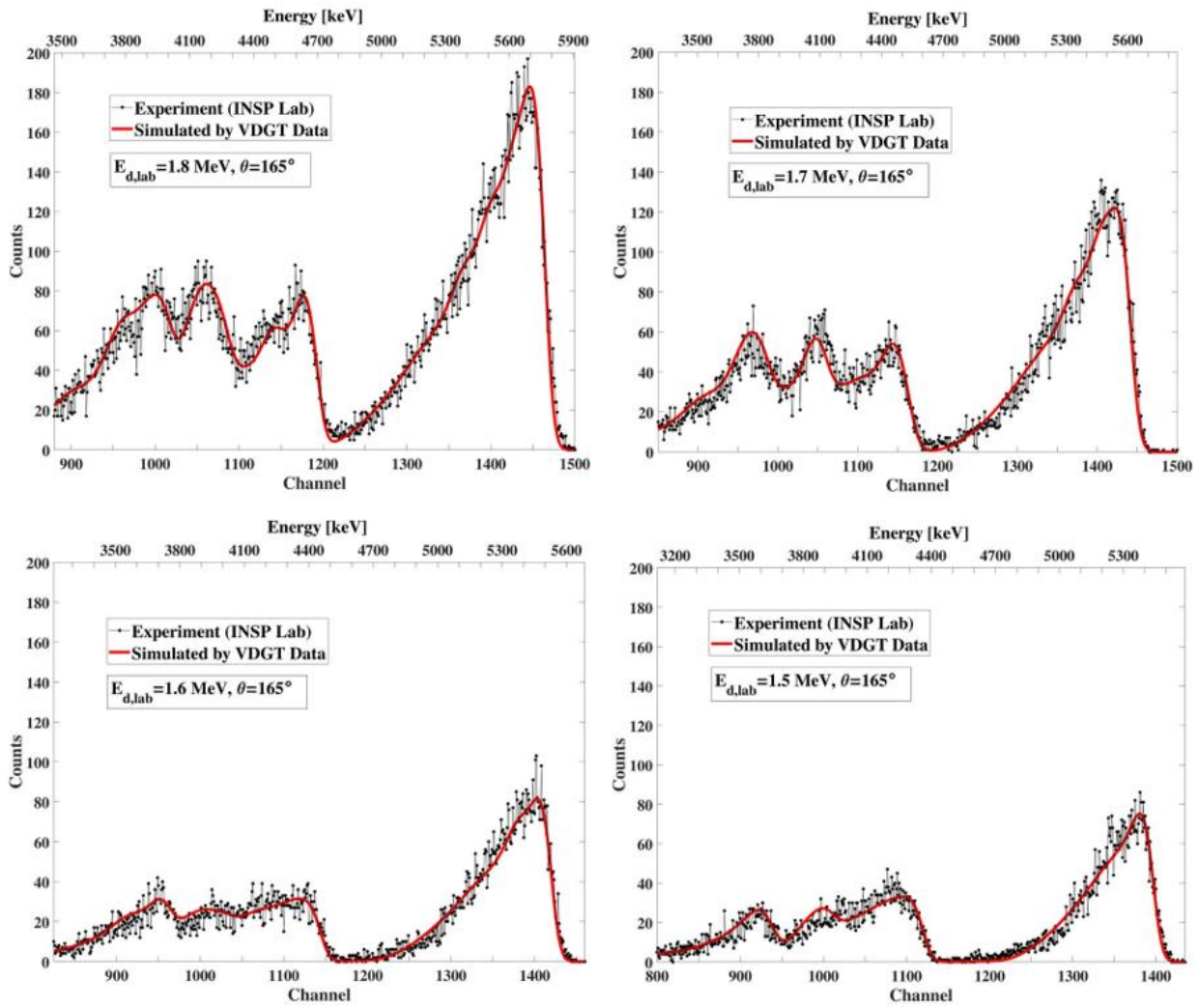


Fig. 19. The benchmarking result at INSP Lab in Paris with measured VDG T data for different incident deuteron energies at 165° .

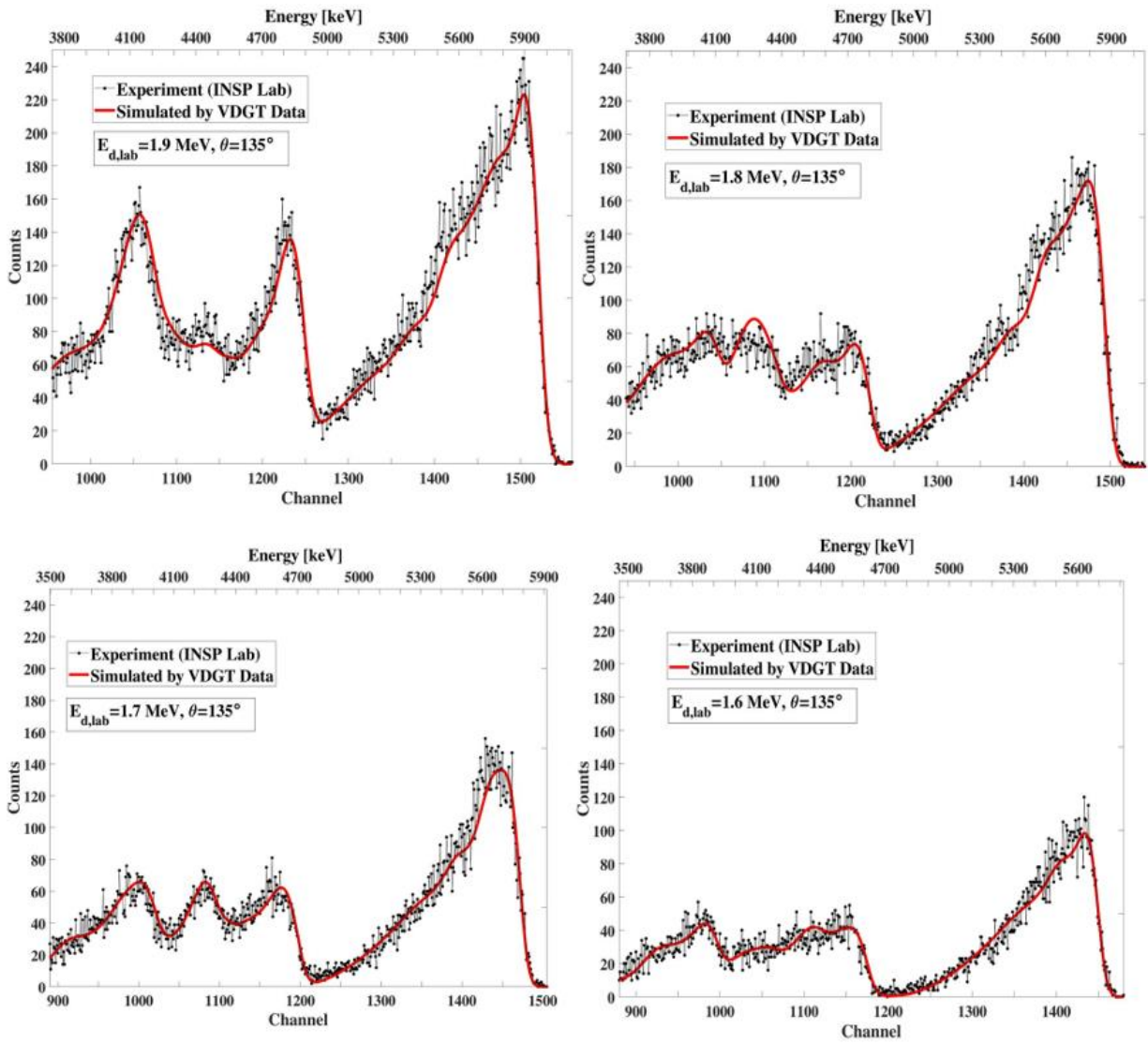


Fig. 20. The benchmarking result at INSP Lab in Paris with measured VDG data for different incident deuteron energies at 135° .

Figures

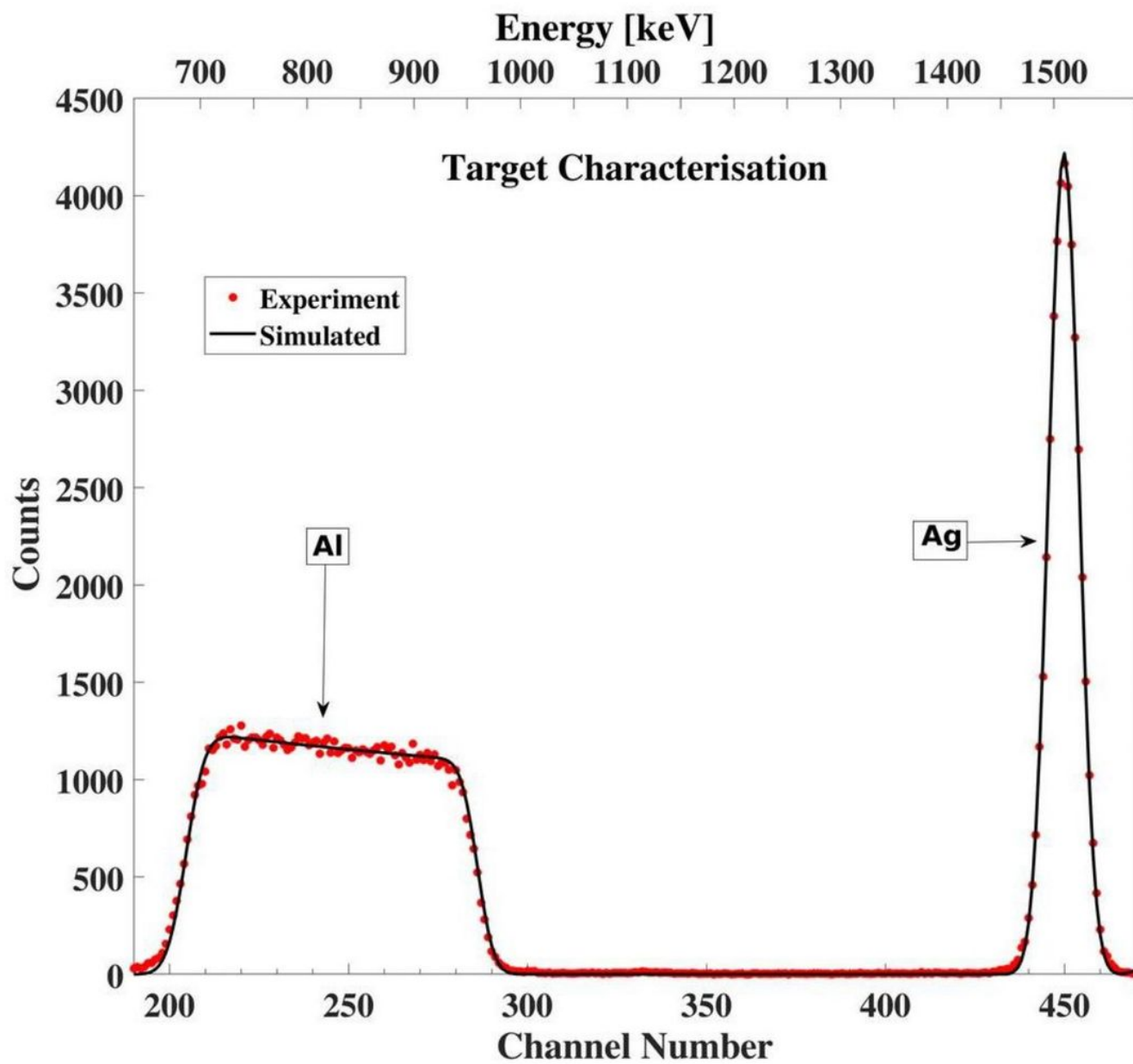
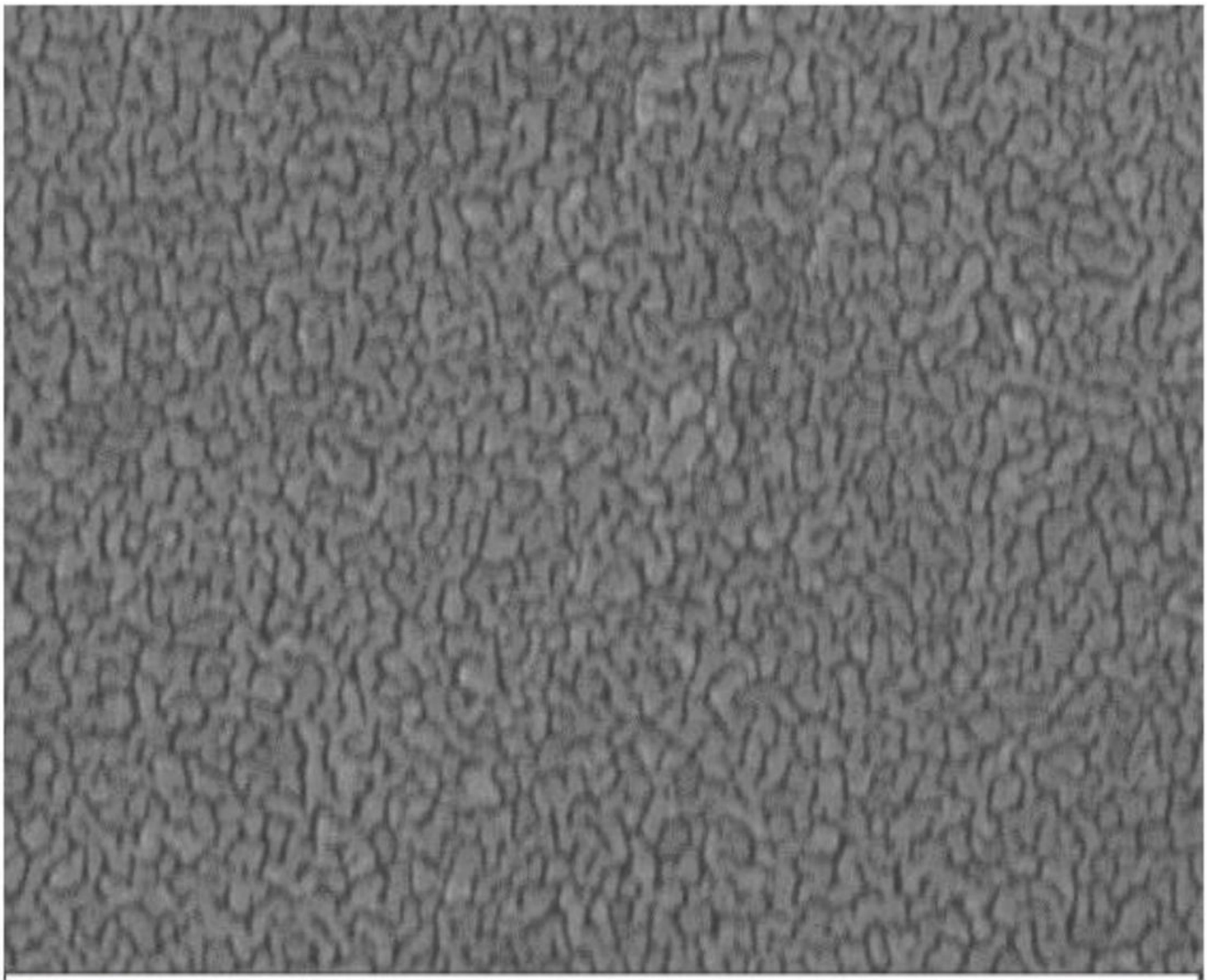


Figure 1

Please see the Manuscript PDF file for the complete figure caption




100 nm

Mag = 80.54 KX
WD = 9.8 mm
Stage at T = 0.0 °

Signal A = InLens
EHT = 20.00 kV
Date : 18 Dec 2020



Figure 2

Please see the Manuscript PDF file for the complete figure caption

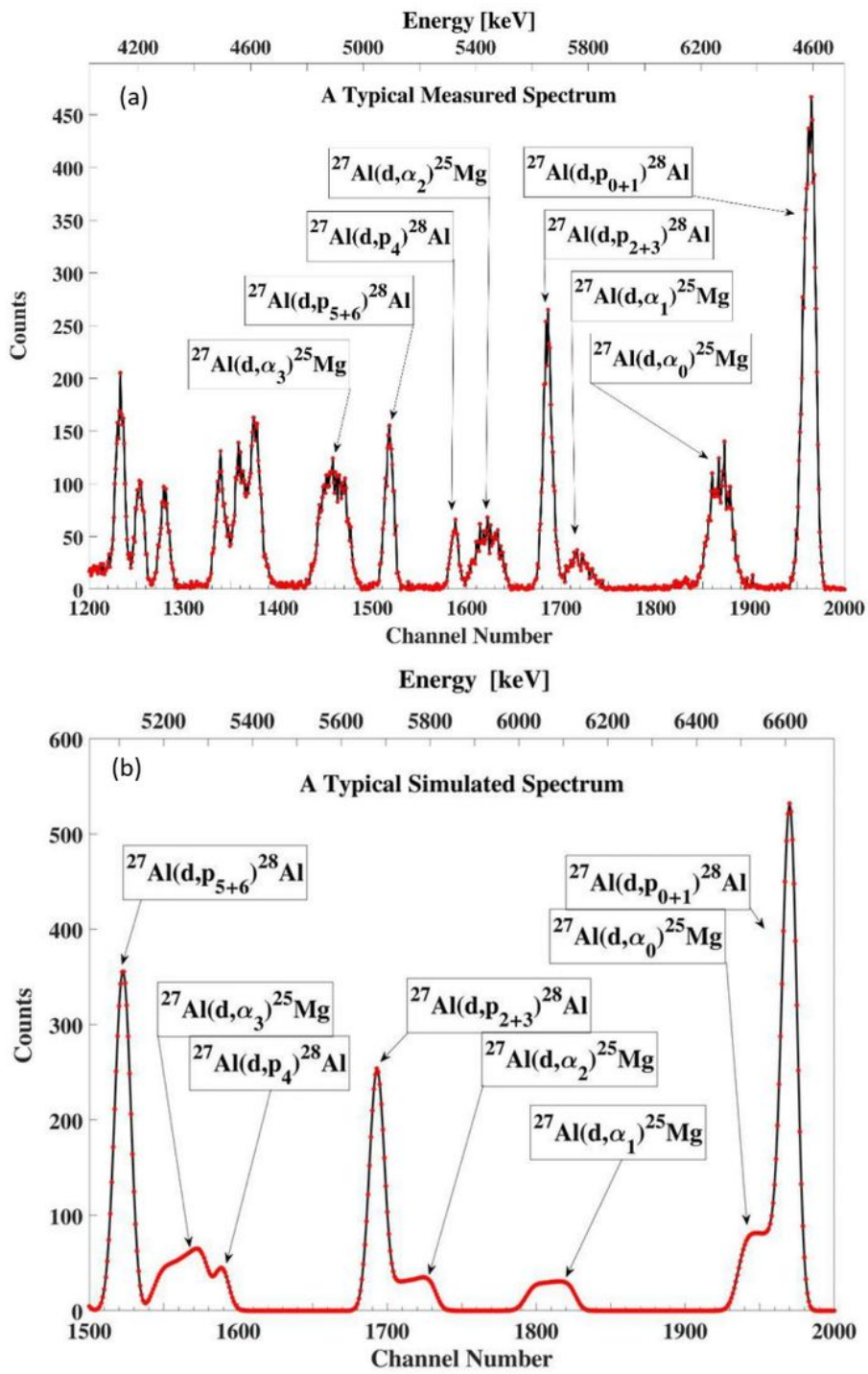


Figure 3

Please see the Manuscript PDF file for the complete figure caption

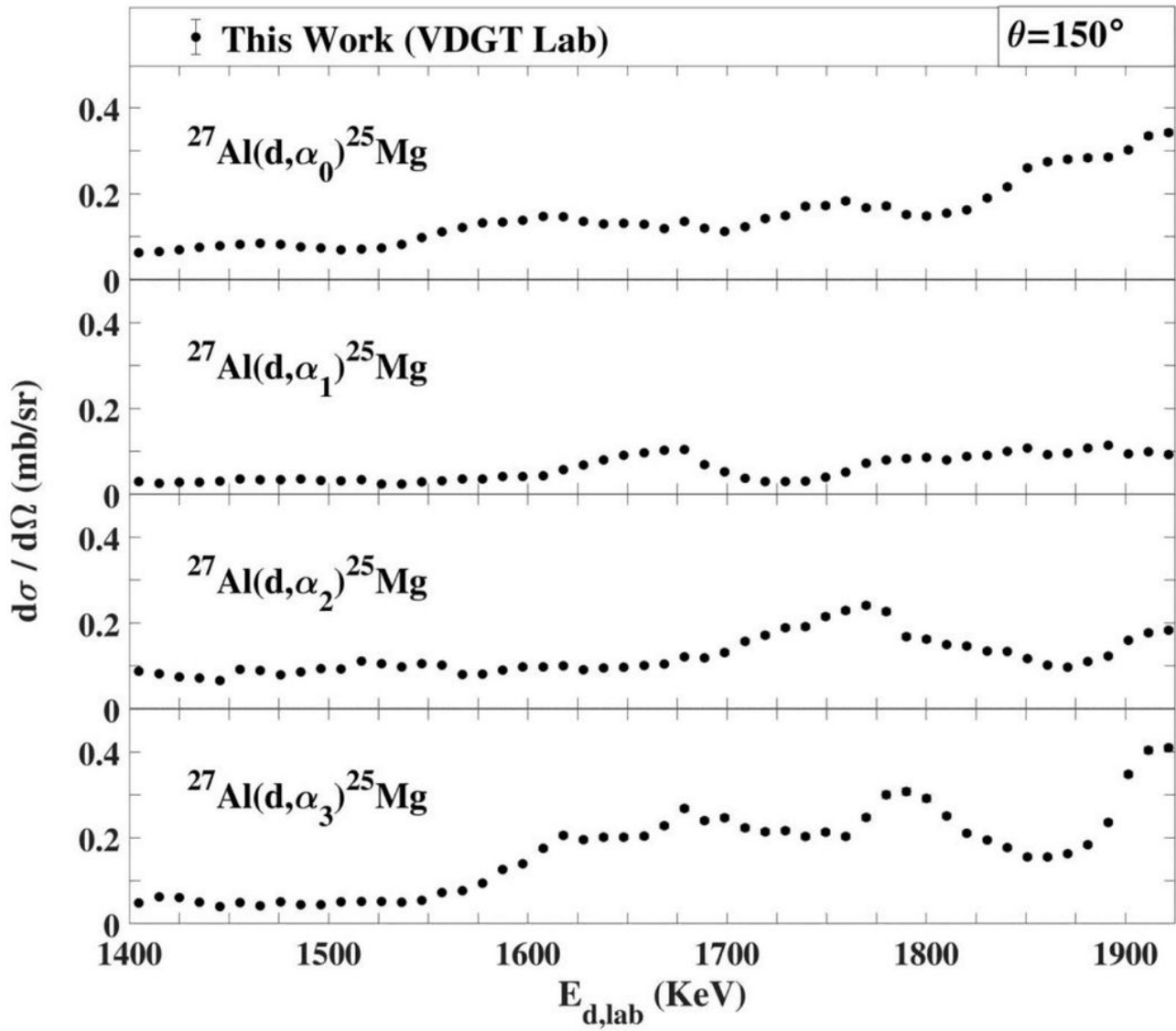


Figure 4

Please see the Manuscript PDF file for the complete figure caption

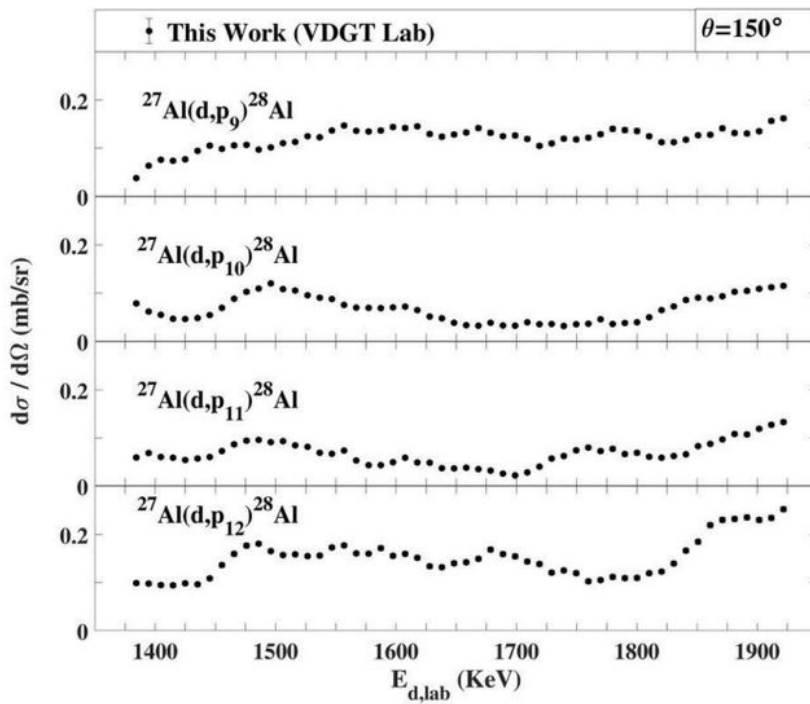
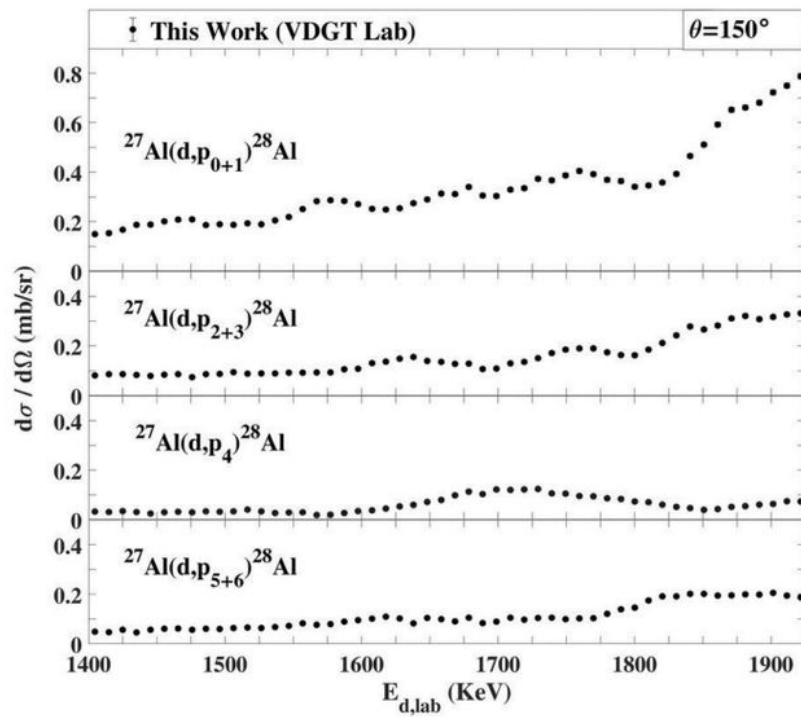


Figure 5

Please see the Manuscript PDF file for the complete figure caption

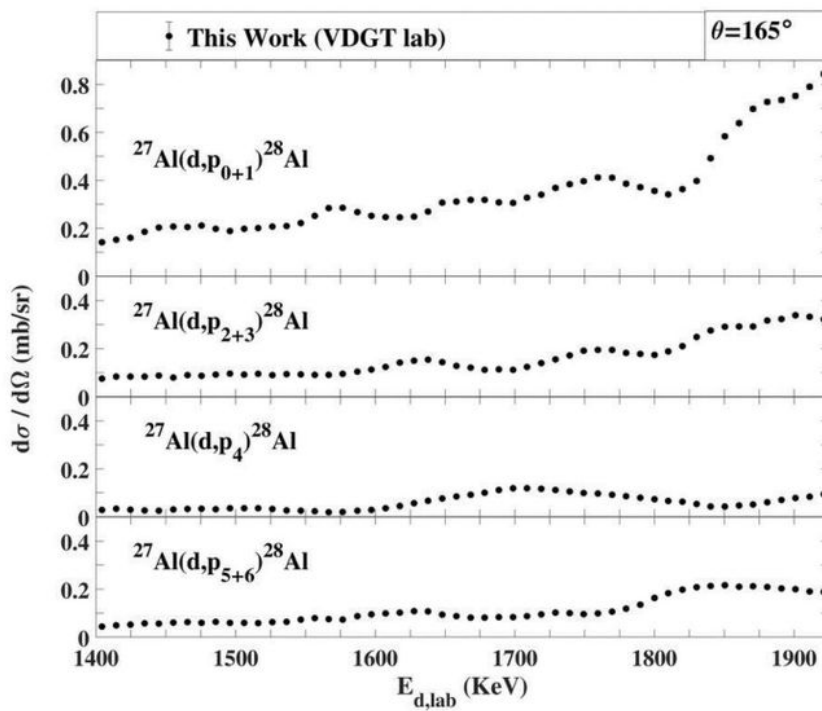
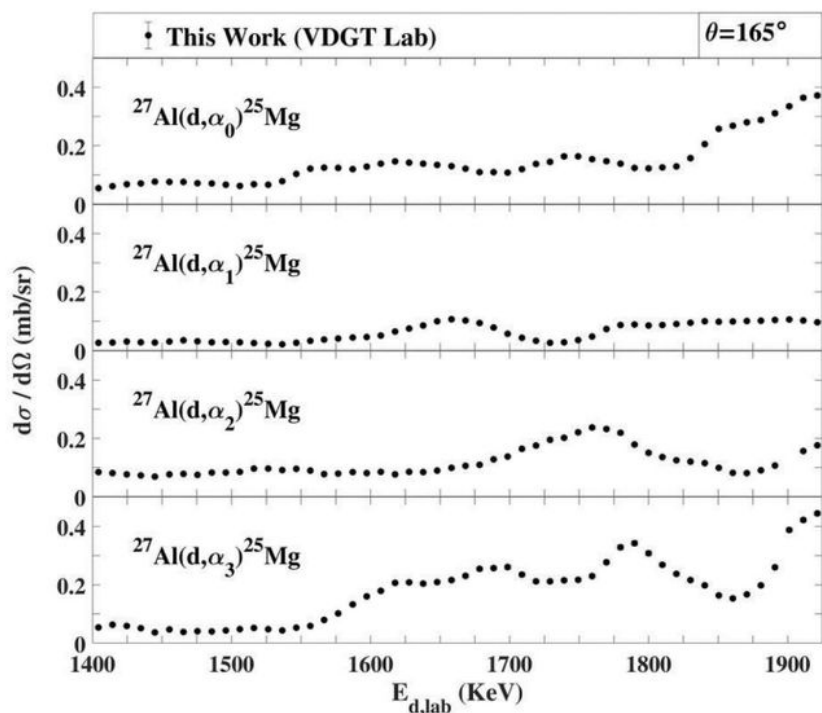


Figure 6

Please see the Manuscript PDF file for the complete figure caption

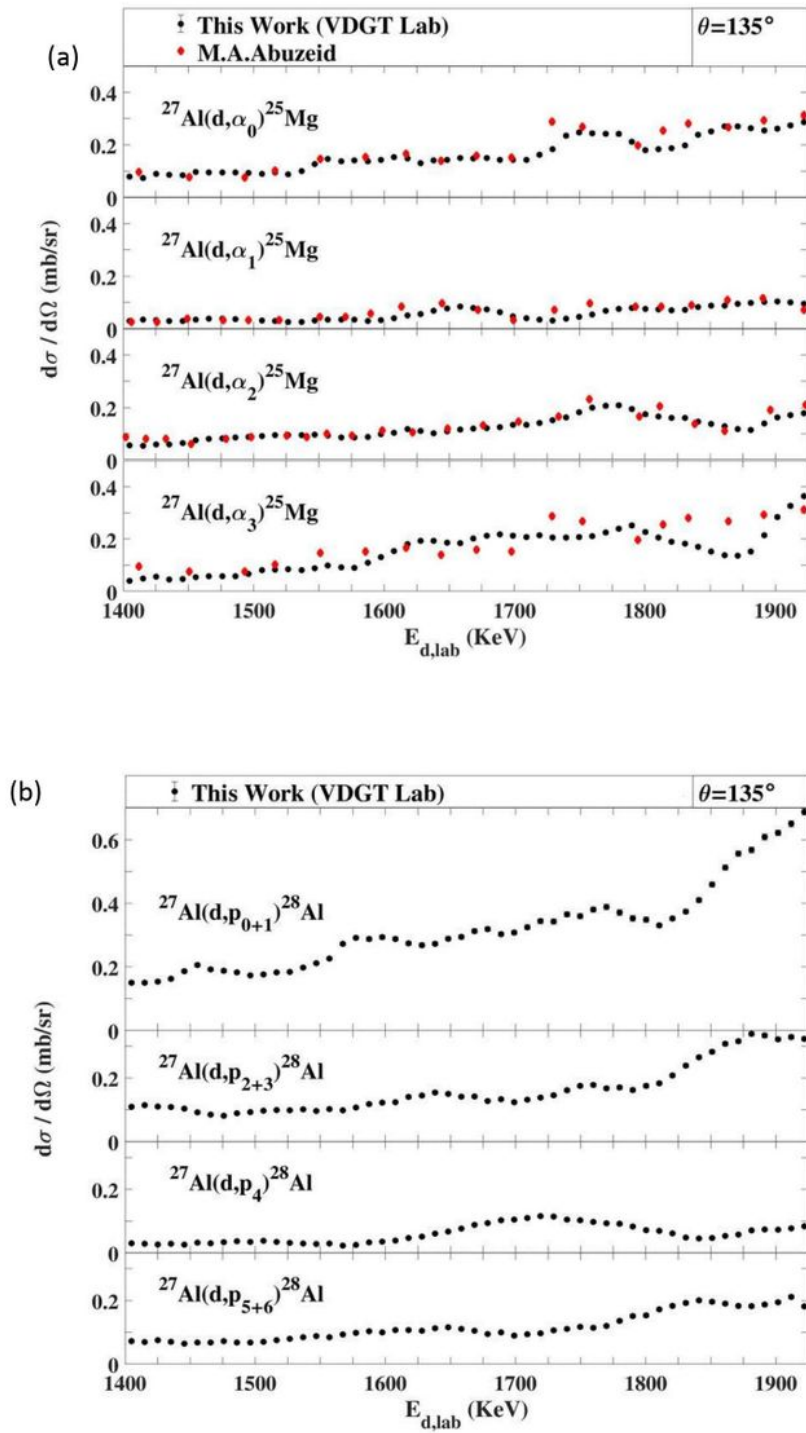


Figure 7

Please see the Manuscript PDF file for the complete figure caption

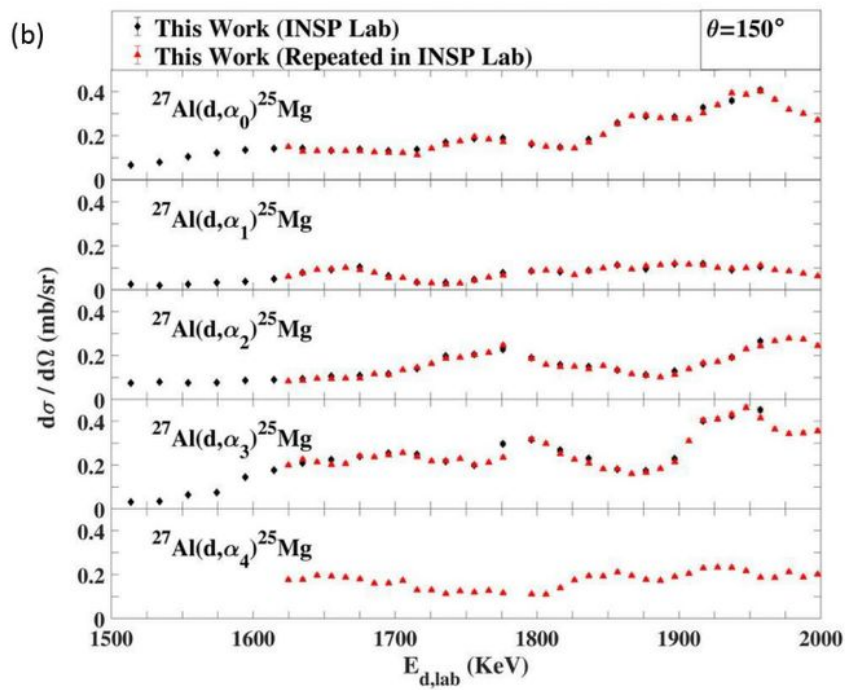
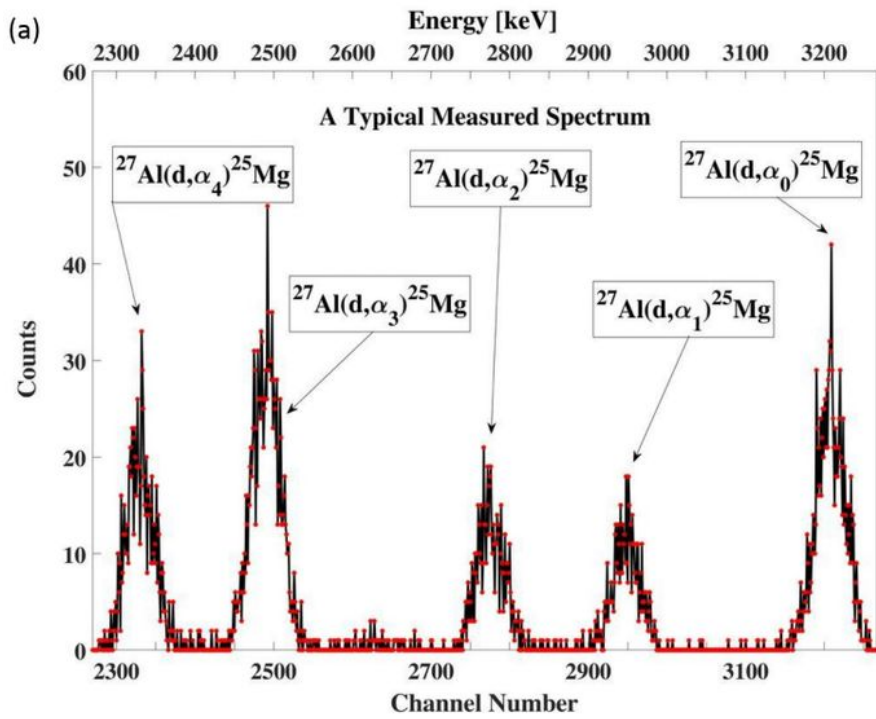


Figure 8

Please see the Manuscript PDF file for the complete figure caption

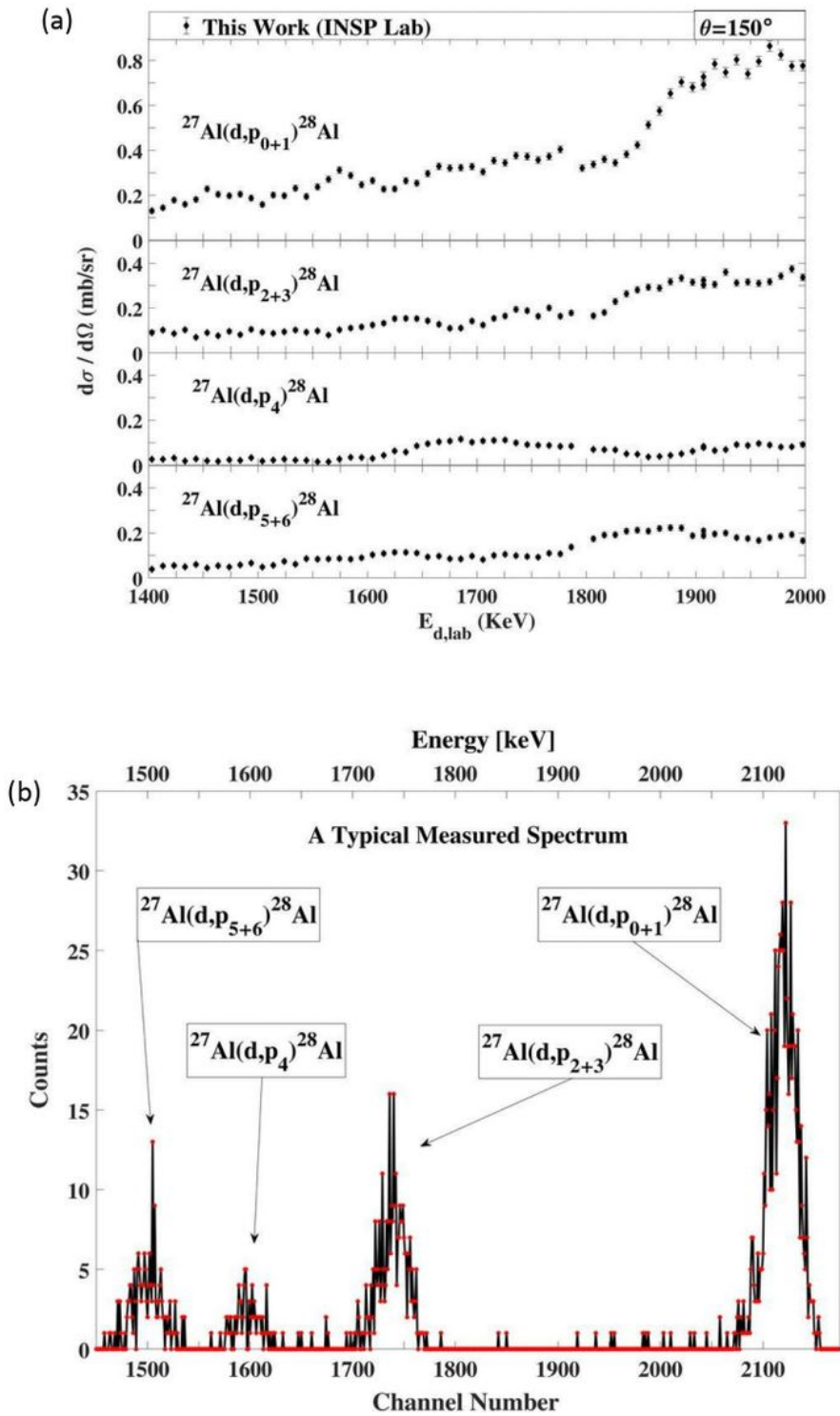


Figure 9

Please see the Manuscript PDF file for the complete figure caption

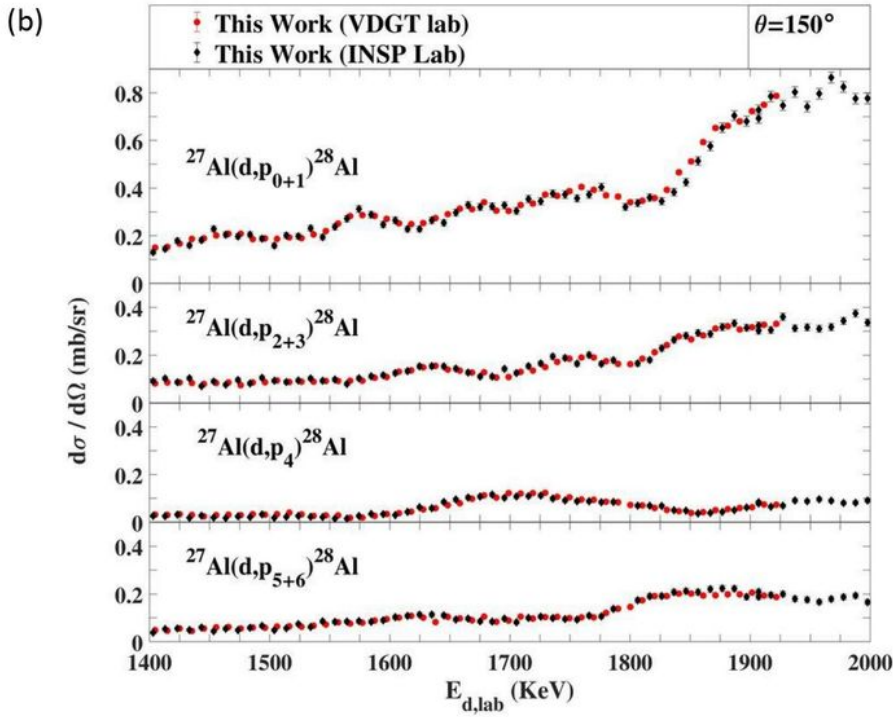
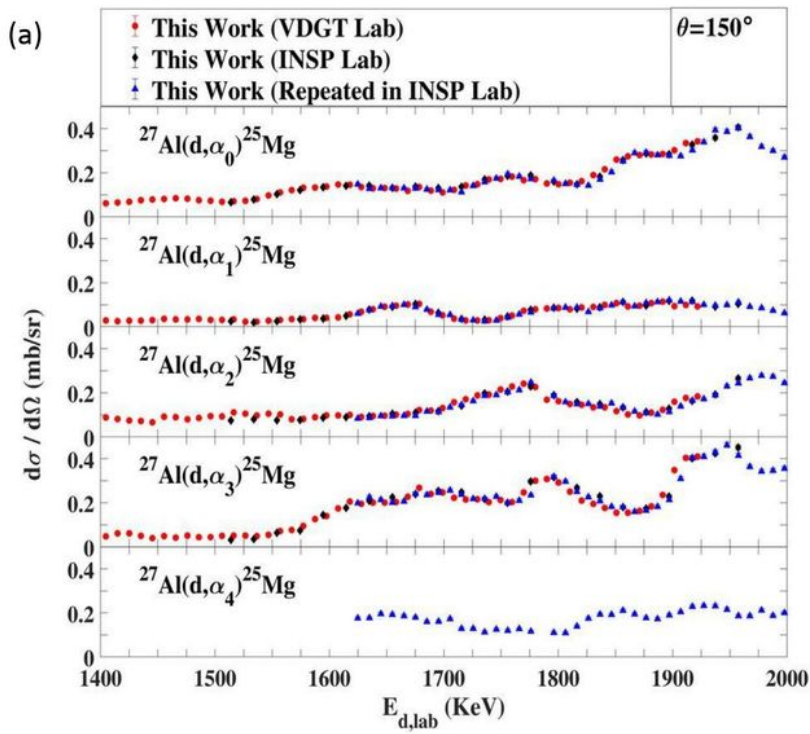


Figure 10

Please see the Manuscript PDF file for the complete figure caption

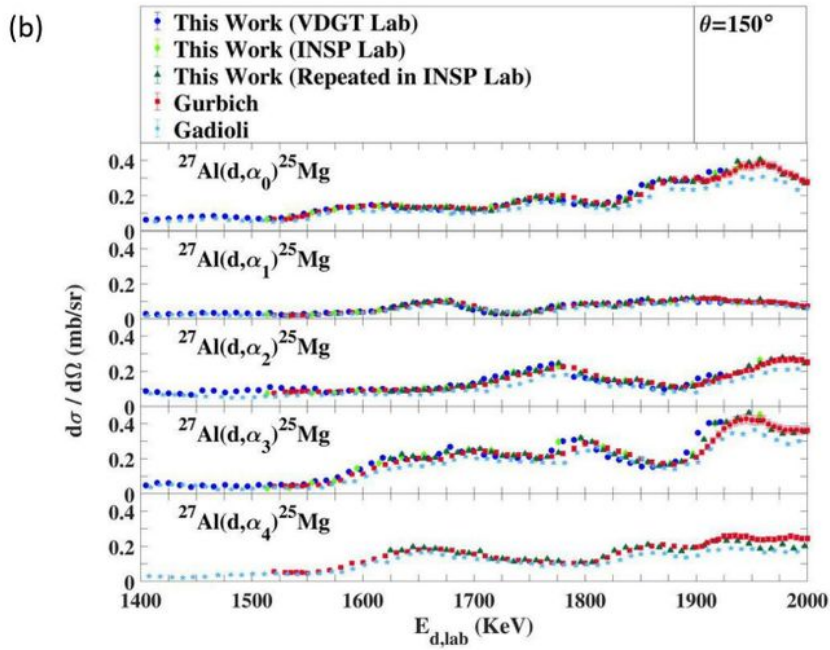
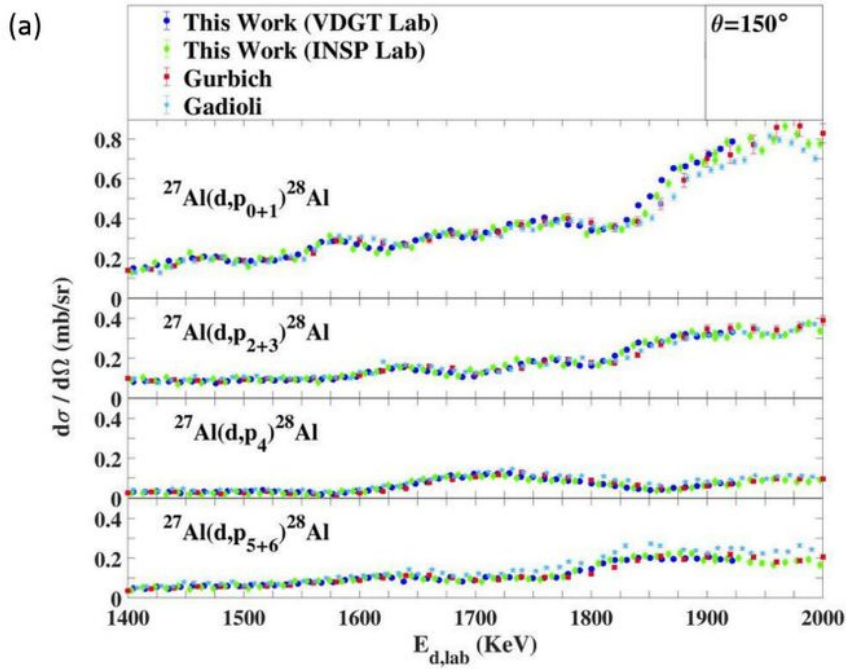


Figure 11

Please see the Manuscript PDF file for the complete figure caption

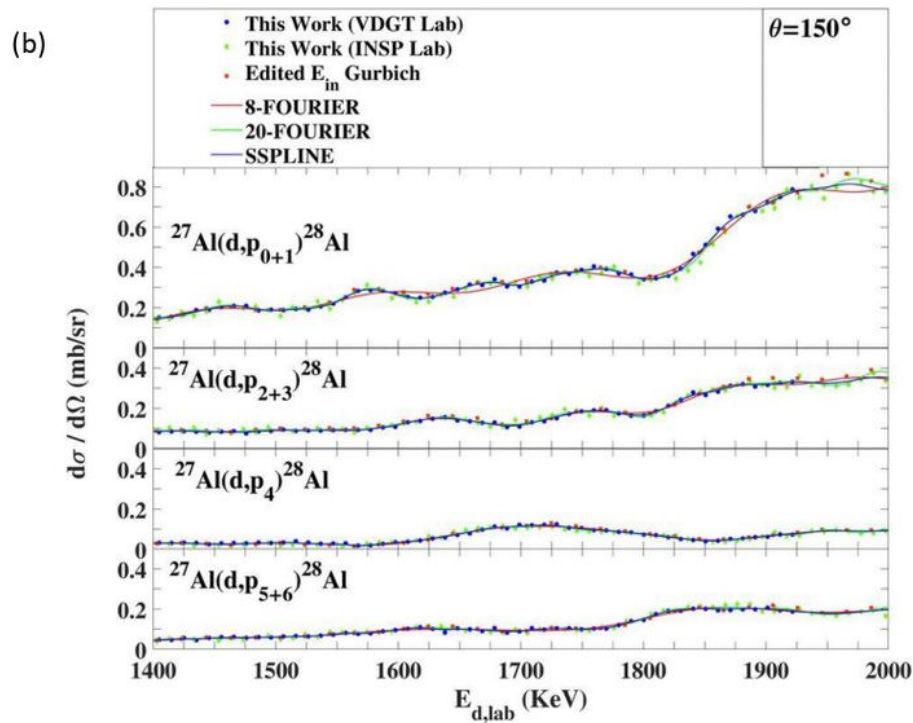
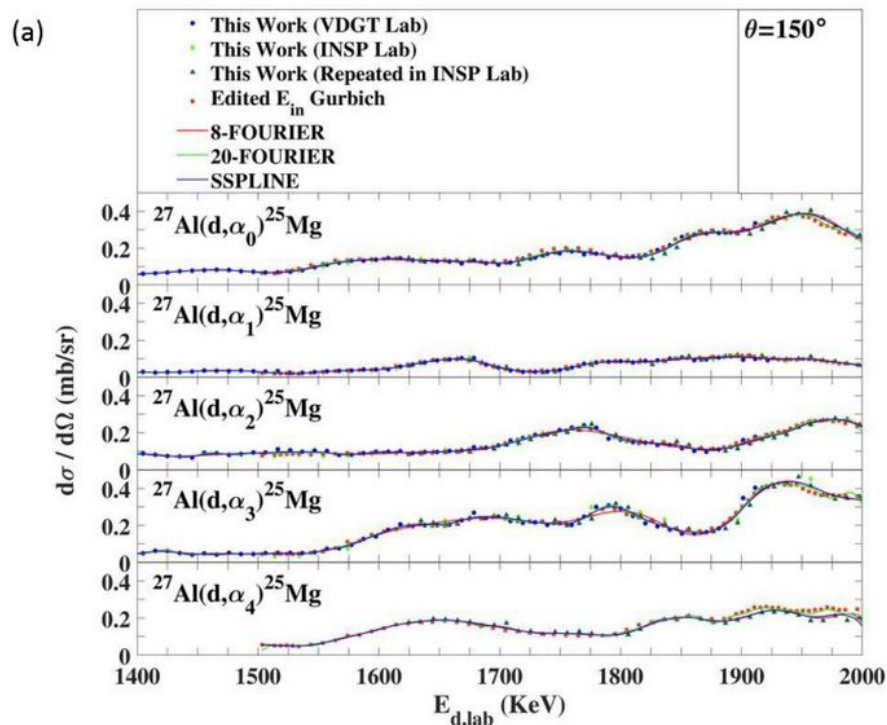


Figure 12

Please see the Manuscript PDF file for the complete figure caption

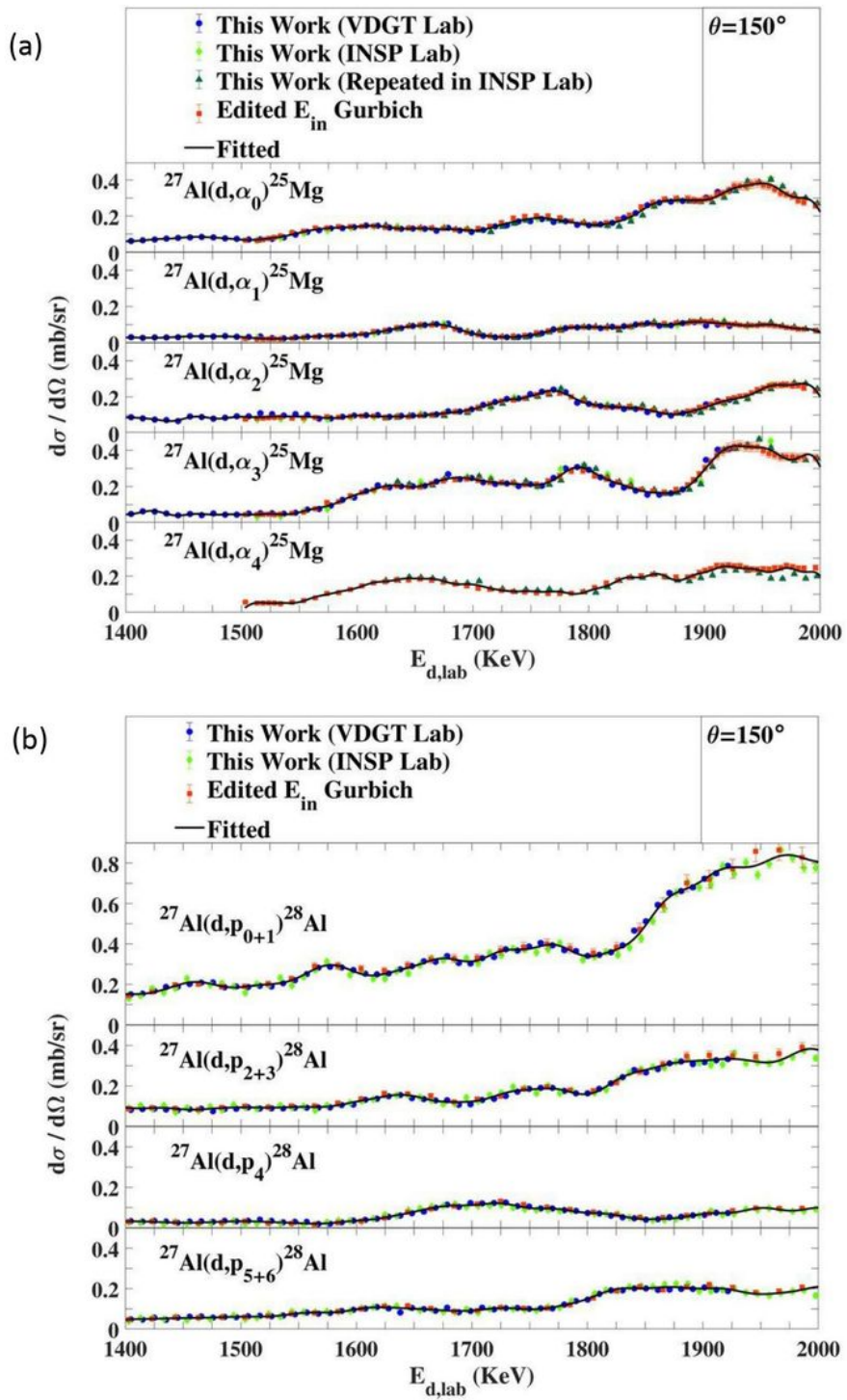


Figure 13

Please see the Manuscript PDF file for the complete figure caption

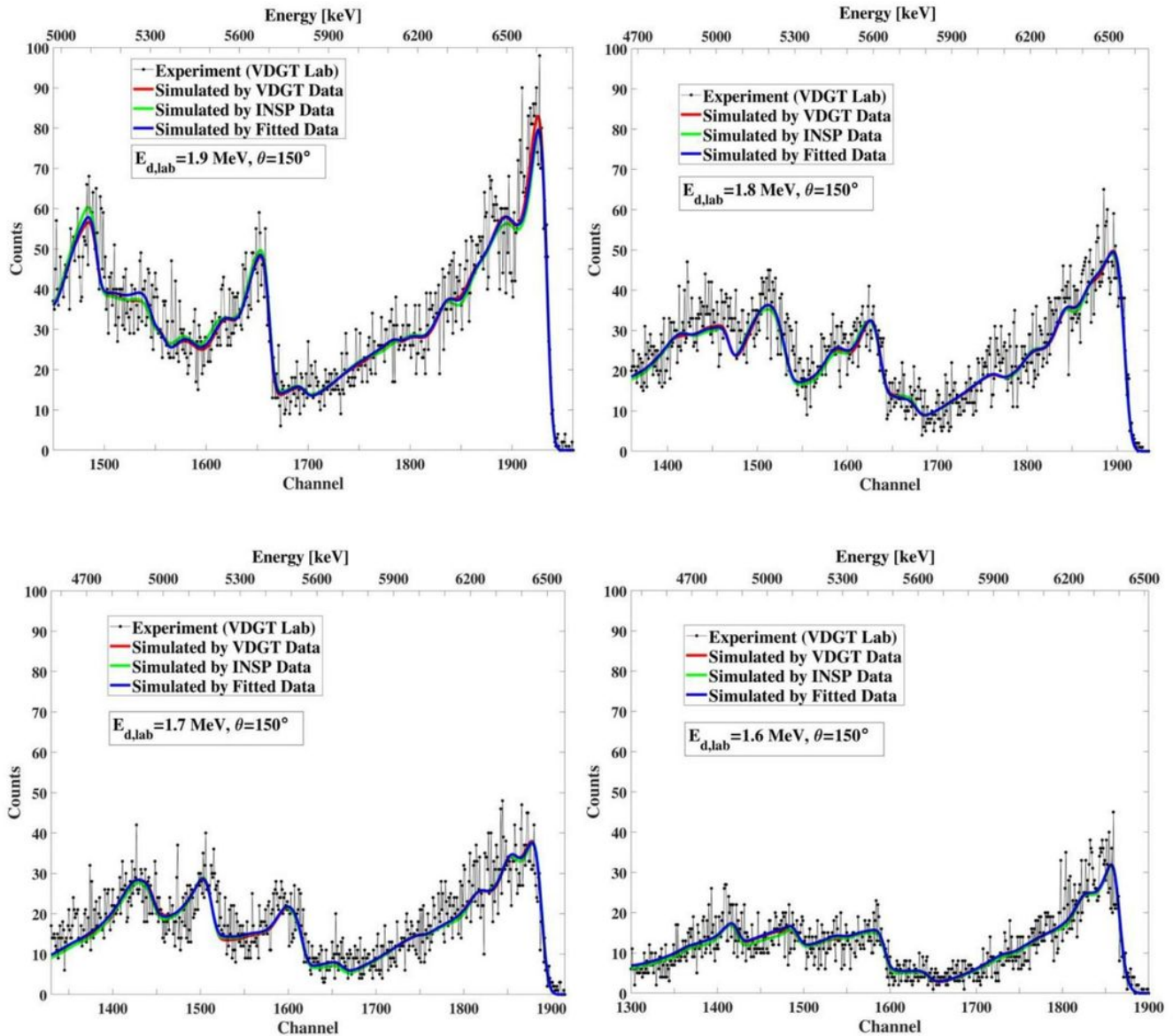


Figure 14

Please see the Manuscript PDF file for the complete figure caption

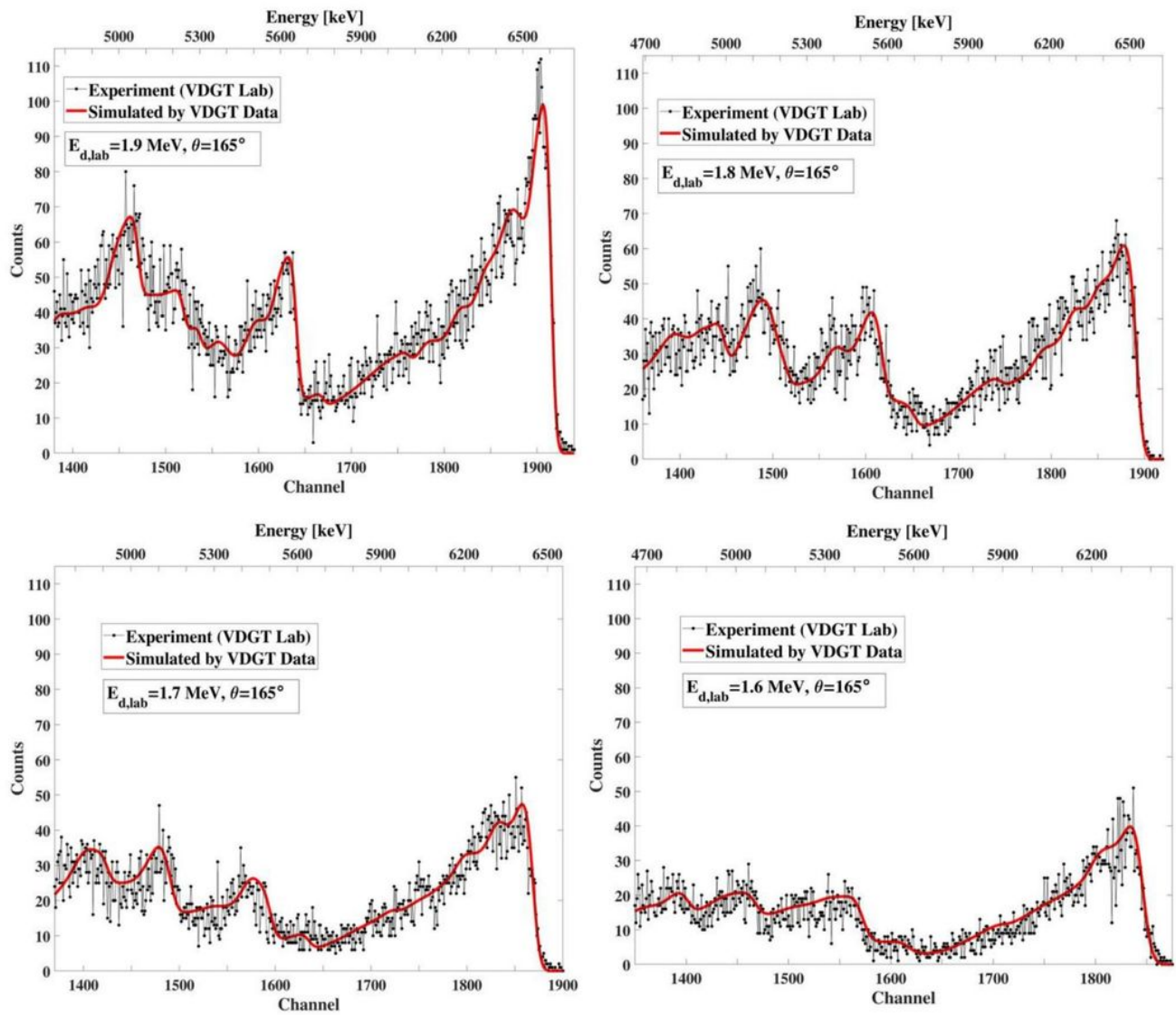


Figure 15

Please see the Manuscript PDF file for the complete figure caption

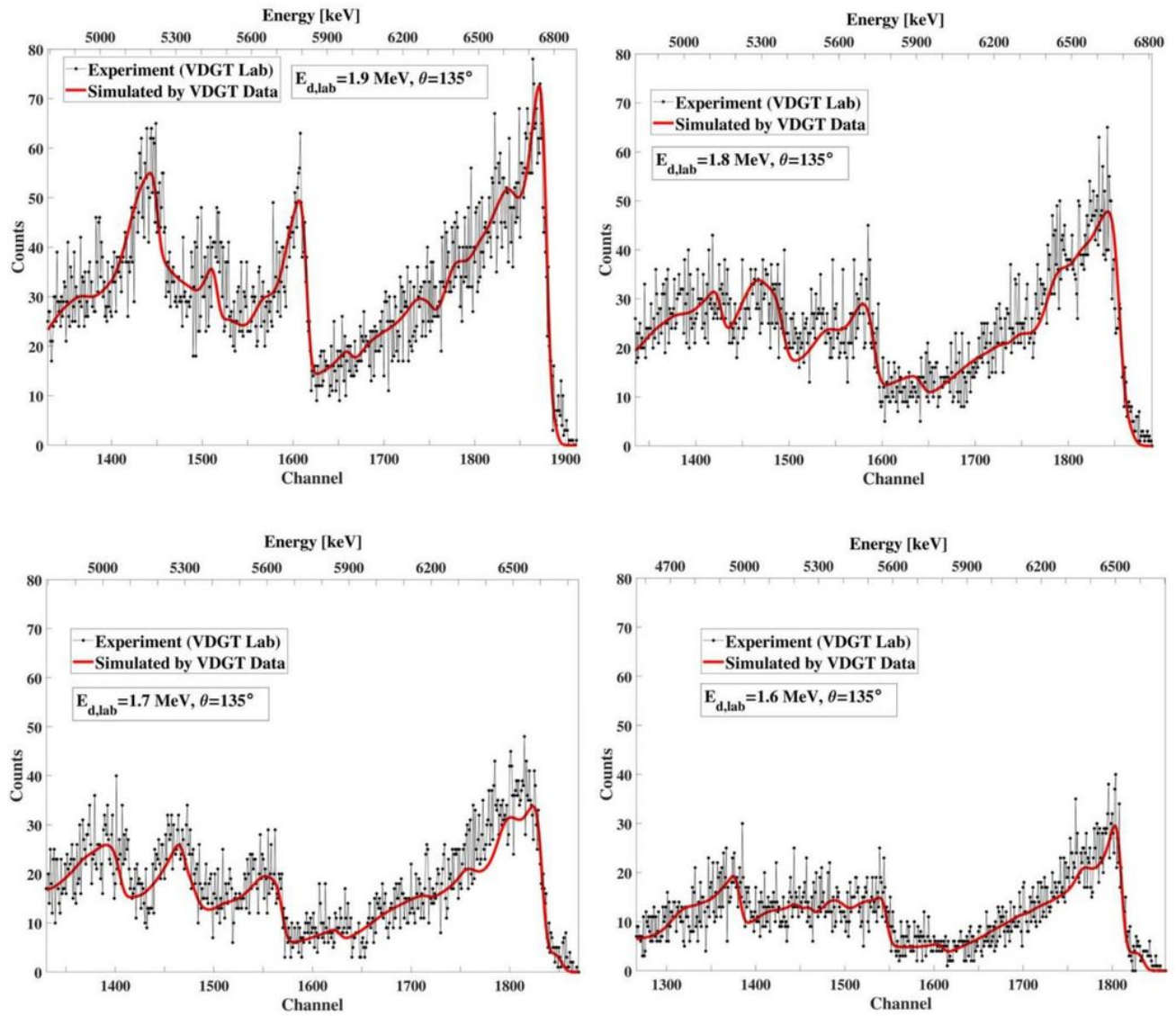


Figure 16

Please see the Manuscript PDF file for the complete figure caption

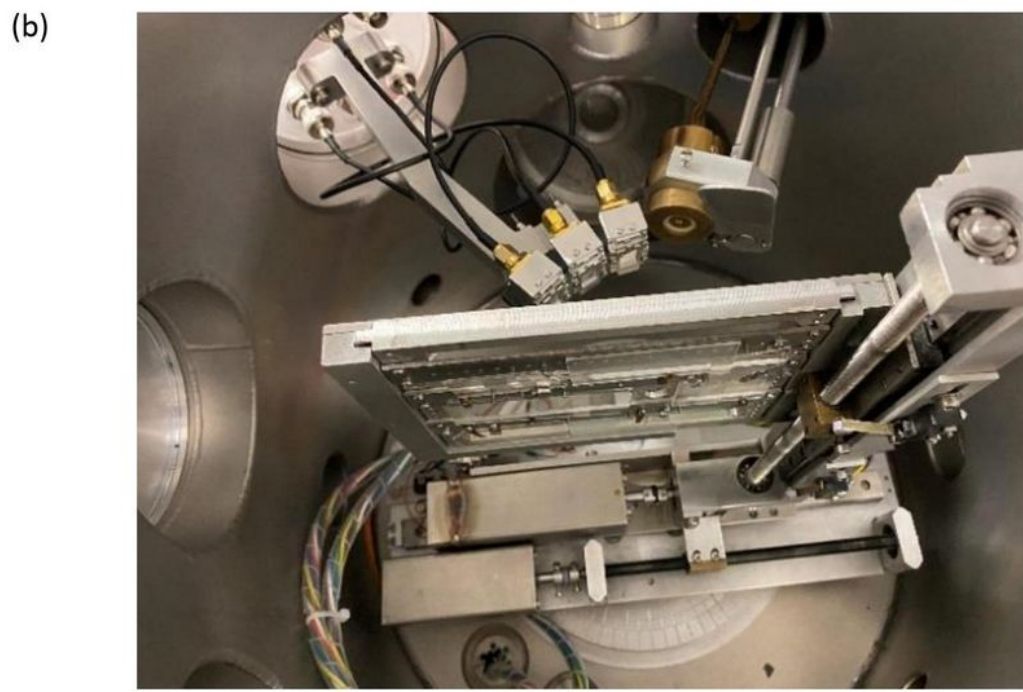
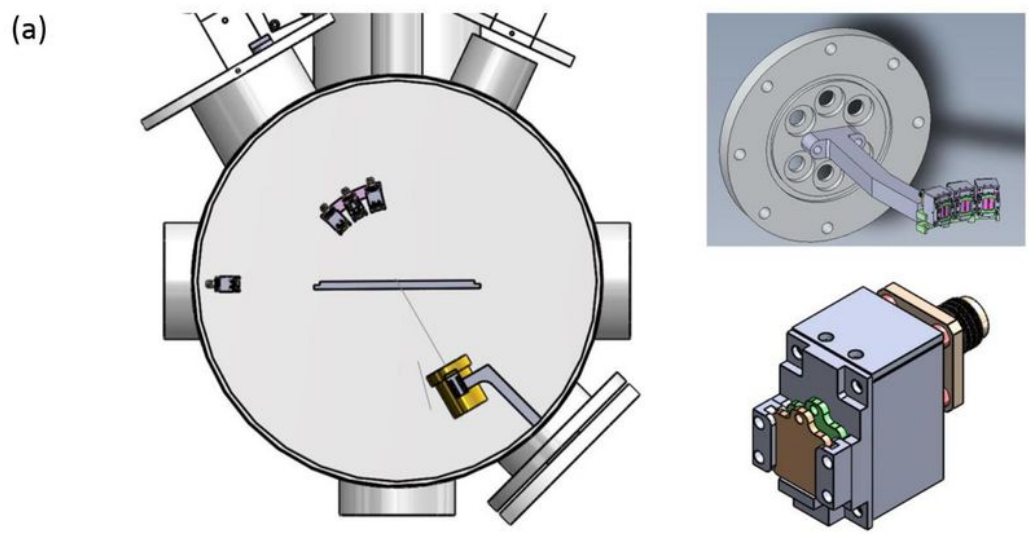


Figure 17

Please see the Manuscript PDF file for the complete figure caption

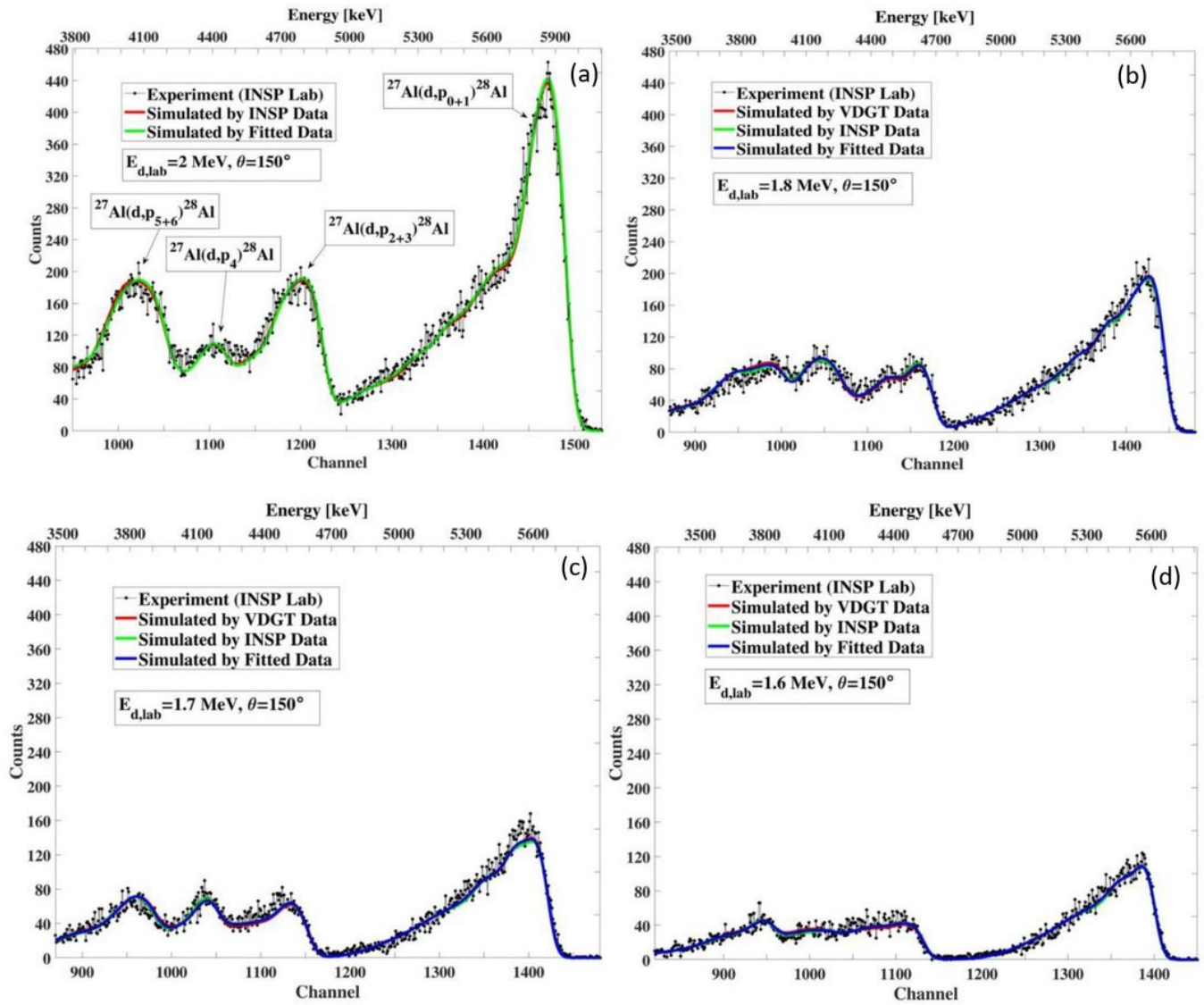


Figure 18

Please see the Manuscript PDF file for the complete figure caption

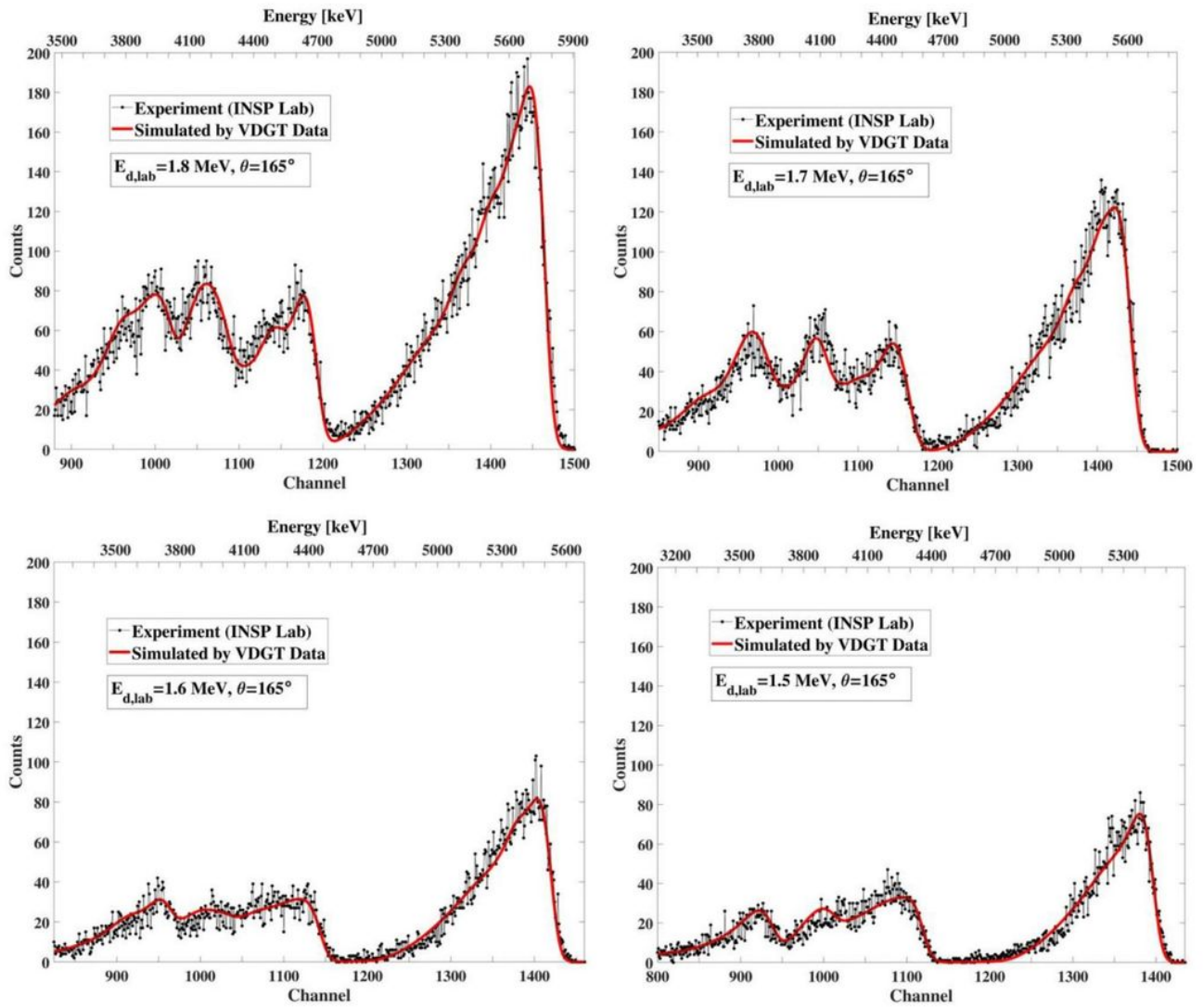


Figure 19

Please see the Manuscript PDF file for the complete figure caption

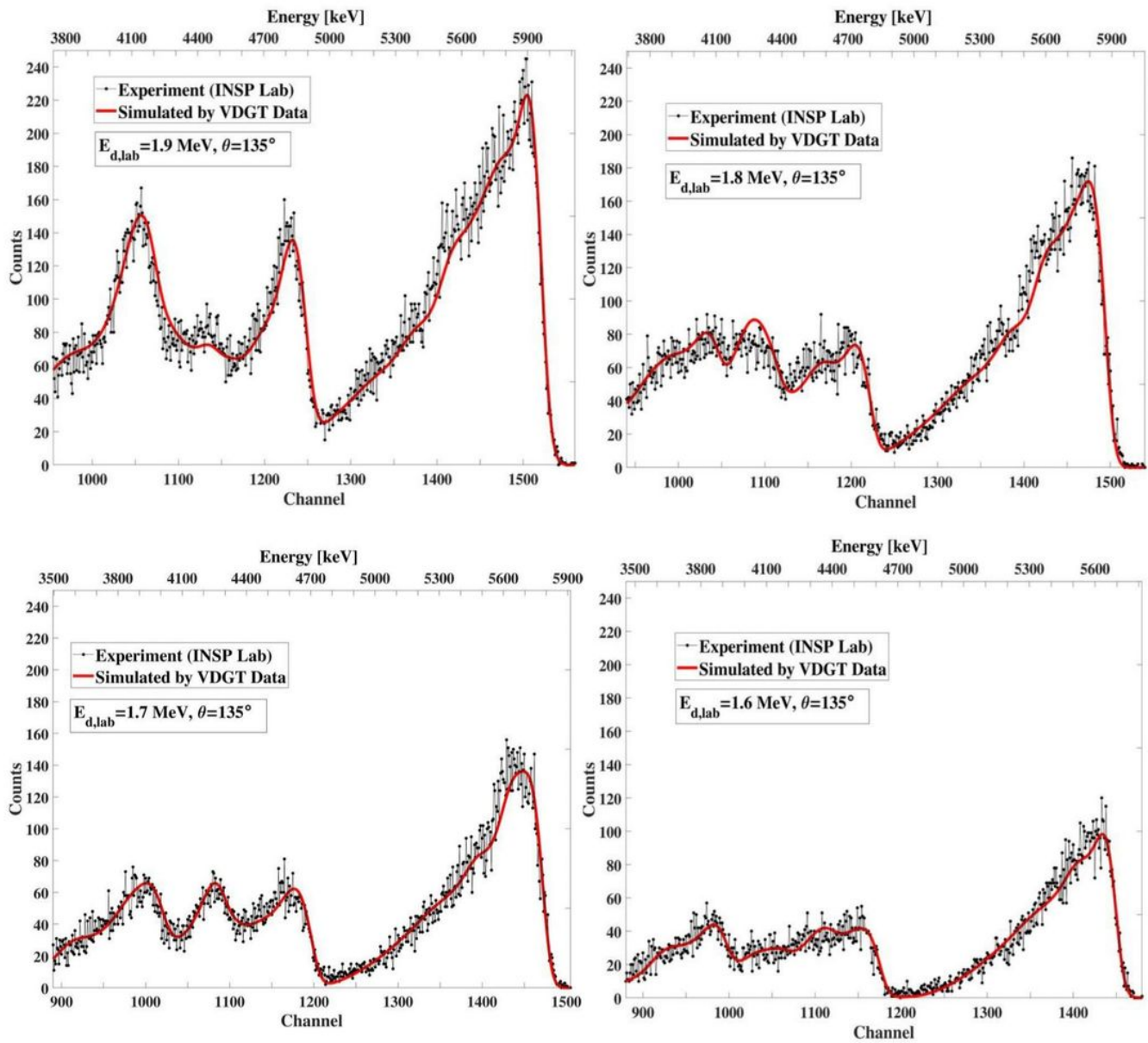


Figure 20

Please see the Manuscript PDF file for the complete figure caption